MAX-PLANCK-INSTITUT FÜR QUANTENOPTIK

State-selective detection of electrostatically guided cold formaldehyde

Markus Schenk

MPQ 317 November 2007

Max-Planck-Institut für Quantenoptik
Hans-Kopfermann-Str. 1
D-85748 Garching, Bundesrepublik Deutschland

State-selective detection of electrostatically guided cold formaldehyde

Diplomarbeit

von

Markus Schenk

Max-Planck-Institut für Quantenoptik
Abteilung Quantendynamik
und
Friedrich-Schiller-Universität Jena
Physikalisch-Astronomische Fakultät
November 5, 2007

1. Gutachter: Professor Dr. G. Rempe
2. Gutachter: Professor Dr. A. Tünnermann

Tag der Verleihung des Diploms : 06.11.2007

Abstract

This thesis reports on state-selective detection of electrostatically guided formaldehyde. Starting from an effusive source of 150 K, slow formaldehyde is velocity-filtered by exploiting the linear Stark effect in an electric field. By this method translationally cold molecules (~ 1 K) are produced. The filtering process also changes the internal distribution of the rotational states. To probe the population of internal states, in a first step room-temperature absorption spectroscopy of two vibronic bands was performed. This allowed us to derive improved molecular constants to calculate transitions frequencies between selected molecular states.

With this knowledge, the rotational distribution of the guided molecules is probed by selectively depleting states with a narrow bandwidth laser. Six states were measured, which sum up to about 30 % of the total molecular flux in the guide. The data agree well with our theoretical expectations, so that the filtering process is now precisely understood. The demonstrated method is well suited for measuring weak transitions. It is applicable in molecular-beam-like experiments and can be used to measure the Stark effect of electronically excited molecules. It is expected that depletion spectroscopy constitutes an important diagnostics in future experiments with translationally cold molecules in individual rotational states.

Zusammenfassung

Diese Arbeit berichtet über zustandselektiven Nachweis von elektrostatisch geführtem kalten Formaldehyd. Ausgehend von einer effusiven Quelle bei 150 K wird langsames Formaldehyd geschwindigkeitsgefiltert durch Ausnutzen des linearen Stark-Effekts in einem elektrischen Feld. Mittels dieser Methode werden translatorisch kalte Moleküle (~ 1 K) erzeugt. Der Filterprozesses ändert auch die interne Verteilung der Rotationszustände. Um die interne Zustandspopulation zu untersuchen wurde in einem ersten Schritt Raumtemperatur-Absorptionsspektroskopie von zwei vibronischen Bändern durchgeführt. Daraus konnten verbesserte Molekülkonstanten bestimmt werde mit denen Übergangsfrequenzen zwischen ausgewählten Zuständen berechnet wurden.

Mit diesem Wissen wurde die Rotationszustandsverteilung der geführten Moleküle untersucht. Dies geschah durch selektives Entvölkern der Zustände mit einem schmalbandigen Laser. Sechs Zustände, die zusammen etwa 30 % des gesamten molekularen Flusses ausmachen, wurden vermessen. Die Daten stimmen gut mit den theoretischen Erwartungen überein, so dass nun der Filterprozess als gut verstanden betrachtet werden kann. Die dargelegte Methode ist zur Messung schwacher Übergänge bestens geeignet. Sie kann in Molekularstrahl-ähnlichen Experimenten angewandt werden und kann den Stark-Effekt von elektronisch angeregten Molekülen bestimmen. Es ist zu erwarten, dass die vorgestellte Methode ein wichtiges Diagnostikwerkzeug für zukünftige Experimente mit translatorisch kalten Molekülen in individuellen Rotationszuständen ist.

Contents

Chapter 1

Introduction

Cold molecules have become a growing field of research in the last decades. The spectacular achievements with cold atoms such as Bose-Einstein condensation [1], high-precision spectroscopy and controllability of single atoms and photons has led to the question what new effects can be observed using molecules at ultralow temperatures. The internal degrees of freedom like rotation and the permanent dipole moment of some molecules promise interesting phenomena. However, laser cooling is not easily applicable for molecules. This difficulty has motivated many researchers to find different approaches to obtain dense samples of cold molecules.

In this work a velocity filter for molecules is characterized by means of spectroscopy. The filter is based on the Stark effect of polar molecules. As the Stark effect depends on the molecular rotational state, different rotational states are filtered with different efficiency. The rotational state distribution after the process of filtering is studied in this work.

The thesis is organized as follows: in this first chapter an overview about the cold molecules research field and current production methods is given. It is followed by chapter 2 that describes the important concepts of theory which are needed in this work. The third chapter describes room-temperature spectroscopy of formaldehyde, which was a necessary step to determine the rotational state distribution of the velocity-filtered beam. This determination of the population is explained in detail in chapter 4. The results are presented in the following chapter 5. The work concludes with a summary and some perspectives of the developed technique (chapter 6).

1.1 Cold molecules research

In this section the most interesting physical questions associated with cold molecules are discussed. First to mention is high-precision spectroscopy with cold molecules. Spectroscopic methods have always a frequency uncertainty due to the limited interaction time of the particles with the light field. Cold molecules have lower velocities and they can therefore increase the accuracy of spectroscopic measurements. The lower velocities of colde molecules can increase the accuracy of spectroscopic measurements by longer interaction times.

Especially interesting is the question of the existence of a finite electric dipole moment of the electron (EDM). This would imply time symmetry violation which is predicted by the Standard modell and several supersymmetrical theories. The order of magnitude of the predicted EDM lies for the Standard modell far beyond any feasible experimental accuracy. But beyond-Standard-modell theories predict it to be in the range of $10^{-25} - 10^{-30}\,\mathrm{e\,cm}$. The experimentally determined upper limit of $|d_e| \leq 1.6 \cdot 10^{-27}\,\mathrm{e\,cm}$ achieved by Regan et. al [2] using atomic Thallium hence could exclude some of these theories. Using molecules like YbF [3] or PbO [4] promises a much higher sensitivity, which can exclude more supersymmetric theories.

Another field of interest is the so called "super-chemistry" or "cold chemistry". Using external parameters as electric and magnetic fields, chemical reactions can be controlled in a coherent way so that the reaction can go deterministically back and forth. As an example a recent paper reports on the observation of coherent oscillations between a molecular state and the state of an atom pair [5]. The question of molecular collisions at low temperatures is interesting, since the molecular de-Broglie wavelength exceeds the classical size of the molecule for low temperatures. During the collision process tunneling and interferences can occur leading to totally new reactions.

The dipole-dipole interaction between polar molecules can be used as a further potential system to construct a quantum computer. Compared to the other proposed interactions it is very long-ranging and therefore promising (see proposal by DeMille [6] and Zoller [7]).

1.2 Production methods

The well established procedure of laser cooling of atoms is not easily adapted to molecules since they lack closed transition due to their rich internal structure. The vibrational transitions do not show strict selection rules as the rotational transitions. After excitation and spontaneous emission the molecular ensemble is in a mixture of different molecular vibrational states. However, some proposals for laser cooling of molecules exist [8, 9, 10] but none has been realized succesfully yet. Therefore alternative methods have been developed in the last decade. All of the used procedures achieving samples of cold molecules can be classified in two methods: indirect and direct methods.

1.2.1 Indirect methods

Indirect methods use ultracold atoms to produce cold molecules. Two indirect methods are known. **Photoassociation (PA)** is a laser-induced formation of molecules [11]. By the absorption of a photon, energy and momentum conservation is fulfilled. The produced molecules are translationally cold but are in a high excited vibrational state. The second indirect method uses **Feshbach resonances**. Those occur if two scattering atoms have a total energy equal to a (quasi-)bound molecular state. The relative energy between the atom and the molecular state can be tuned on resonance via magnetic field change, since the different states have different magnetic moments. By adiabatically changing the magnetic field from one side of the resonance to the other side, one can transfer the population from atoms into molecules [12]. With this technique molecular BEC's have been realized [13].

1.2.2 Direct methods

Direct methods use room-temperature molecules and cool them down. The first successfully implemented idea below 1 K was **buffer-gas cooling** with helium in the Doyle group. The buffer-gas cooles the molecules via collisions. Since helium is still gaseous at 5 K it is used. Buffer-gas cooling of CaH molecules and trapping in a magnetic field configuration at 400 mK was achieved [14]. The lifetime in the trap, however, is severely reduced by the high background pressure of He. This limits the use of the magnetic trap for evaporative cooling schemes. The advantage of buffer-gas cooling is its general applicability to many molecules. The main restriction to the molecules is only that they are stable under collisions with helium.

Another method is **supersonic-beam expansion** of a molecular gas. A gas at very high pressure is ejected out of a nozzle. Caused by adiabatic expansion in and behind the nozzle, the internal degrees of freedom, rotation and vibration, are cooled down. The longitudinal velocity is very high but has a narrow distribution. The molecules are skimmed and therefore in the transverse direction slow. The narrow velocity distribution must now be transferred into the lab frame. The main method for this is **Stark deceleration** developed in the Meijer group [15]. Molecules that are in a low-field seeking state are decelerate by moving towards higher electric fields. When they pass the electrode, it is switched to low electric fields, so that the molecule is not accelerated. The molecules can be brought to halt by extending this scheme to many subsequent electrodes. This technique is inherently pulsed.

Very analogous is the **optical Stark deceleration** [16]. A 1-D optical lattice of intense far-off resonant light is copropagating with the molecular beam. The molecules are decelerated by adjusting the lattice velocity. Nitric oxide has been decelerated from 400 m/s to 290 m/s within a 6 ns short pulse.

The method used in this work is a **velocity filter** for molecules based on the Stark effect. It exploits the fact that slow molecules are present at a small fraction even at room-temperature gas. Slow molecules in a low-field seeking state are guided in an electric quadrupole field while the fast molecules and those in high-field seeking state are lost. This filter works well with polar molecules since only molecules with a permanent dipole moment can have a linear Stark shift and feel the quadrupole field as sufficiently strong potential. This results in a source of translationally cold molecules with a flux up to $\approx 10^{10}$/s and typical average longitudinal velocities of about 50 m/s. The state-distribution of this molecular beam is expected to depend on the Stark shift and on the occupation of the rotational state in the thermal source. This work studies this distribution experimentally.

Chapter 2

A short story of rotational molecular spectra

In this chapter the main theoretical background for this work will be pointed out. It starts with the Born-Oppenheimer approximation, which separates the nuclear motion from electronic motion. This allows us to discrminiate between different energy contribution of the total molecular energy. This will be specialized to the calculation of the rotational energies of a general asymmetric molecule. The vibrational normal modes of molecules are introduced with formaldehyde as example. It concludes with a short comment about centrifugal distortion of rotating molecules.

2.1 Born-Oppenheimer approximation

The total energy of a molecule is determined by the Hamiltonian consisting of various interaction and energy terms:

$$H = T_e + T_n + V_{ee} + V_{nn} + V_{en} \tag{2.1}$$

where T_e and T_n is the kinetic energy of electron and nuclei, V_{ee}, V_{en} and V_{nn} are the interaction terms of electrons and nuclei.

To solve the Schrödinger equation with the Hamiltonian 2.1, the Born-Oppenheimer (BO) approximation is a widely used method in quantum chemistry. It consists of two basic steps.

First the electronic Schrödinger equation is solved. It consists of the molecular Hamiltonian but the nuclear terms T_n and V_{nn} are subtracted.

$$H_e \psi_e^R(r) = E_e(R) \psi_e^R(r) \quad , \tag{2.2}$$

with H_e as the electronic Hamiltonian, $\psi_e^R(r)$ is the electron wavefunction as function of the i electrons position $r = (r_1, ...r_i)$ and $R = (R_1, ..., R_n)$ as position parameter of the n nuclei. The solution of this Schrödinger equation yields the energy eigenvalues $E_e(R)$ of the system as a function of the nuclei coordinates R. The electronic wavefunctions ψ_e are in general not only dependent on the positions of the nuclei but also on their velocities. As one assumption of the BO this can be neglected due to the higher mass of the nuclei and hence their smaller velocity compared to the electrons. $E_e(R)$ is called the potential energy surface of the molecule.

In the second step of the BO approximation the nuclear kinetic energy T_n is reintroduced into the Schrödinger equation, but now with the solutions $E_e(R)$ also plugged in:

$$(E_e(R) + T_n)\phi(R) = E\phi(R) \tag{2.3}$$

The kinetic energy part of the Hamiltonian T_n can be split into three parts: the centre of mass kinetic energy T_c, the vibrational energy of the nuclei H_{vib} and the rotational energy of the nuclei H_{Rot}. The $\phi(R)$ can as further approximation be written as a product of wavefunctions of the rotational and vibrational term. For this work only the rotational term of the wavefunction is important and will be considered in the next section.

2.2 Rotational energy levels

The rotational Hamilton operator of a molecule in the rigid rotor approximation (i.e. the internuclei distances are fixed, valid for low J‘s and no vibrations. See section 2.4 for comment about non-rogid rotors) is given in the principal moments of inertia frame as

$$H_{Rot} = \frac{1}{2}\left(\frac{P_x^2}{I_x} + \frac{P_y^2}{I_y} + \frac{P_z^2}{I_z}\right) \tag{2.4}$$

with the angular momentum operator usually in spectroscopy labelled by P_i and I_i as the moment of inertia in direction of $i \in (x, y, z)$. The principal moments of inertia are ordered alphabetically in increasing size : $I_a \leq I_b \leq I_c$. a, b, and c are the the molecular axes.

2.2.1 Symmetric rotor

The symmetric rotor is defined as a body with two equal pricipal moments of inertia. If these are bigger than the third one we call it prolate symmetric rotor ($I_a < I_b = I_c$), in the other case its an oblate symmetric rotor ($I_a = I_b < I_c$)(see Fig. 2.1).

For the symmetric rotor we can rewrite (2.4) to

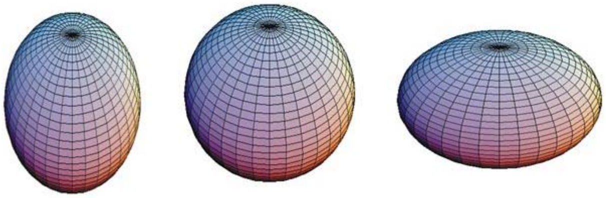

Figure 2.1: *Moment of inertia ellipsoid for the oblate (left), spherical (middle) and prolate (right) case of the symmetric rotor.*

$$H_{Rot} = \frac{1}{2}\left(\frac{1}{I_x}\left(P^2 - P_z^2\right) + \frac{P_z^2}{I_z}\right) \tag{2.5}$$

with $I_x = I_y$.

To find now the rotational wavefunctions of the symmetric rotor, one has to look at the commutation relations between the Hamiltonian and the angular momentum operators. Similar to the H-Atom we find by using (2.5) the following relations:

$$[H, P_z] = 0 \qquad [H, P^2] = 0 \qquad [H, P_Z] = 0 \tag{2.6}$$

(z: quantization axis in the molecular fixed frame, Z: quantization axis of the laboratory fixed frame and $H = H_{Rot}$). These relations represent the fact that all three observables are constants of motion of the molecule. All three operators have therefore the same eigenfunctions which we denote with $|\psi_{J,K,M}\rangle$ or short $|JKM\rangle$ and the eigenvalue equations:

$$\langle JKM|P^2\,|JKM\rangle = \hbar^2 J(J+1) \tag{2.7}$$
$$\langle JKM|P_z\,|JKM\rangle = \hbar K \tag{2.8}$$
$$\langle JKM|P_Z\,|JKM\rangle = \hbar M \tag{2.9}$$

J is the angular momentum quantum number, K the projection of the angular momentum onto the z-axis and M the projection onto the Z-axis.

The energy levels of the symmetric rotor can then be calculated by using (2.5) and the eigenvalue equations (2.7) and (2.8):

$$E_{J,K} = BJ(J+1) + (A-B)K_-^2 \quad (prolate\, B = C) \tag{2.10}$$
$$E_{J,K} = BJ(J+1) + (C-B)K_+^2 \quad (oblate\, A = B) \tag{2.11}$$

Note: The energy levels are twofold degenerate (because of K^2). K_- denotes the quantum number K for the prolate case, K_+ respectively for the oblate case. A, B and C are the rotational constants used in spectroscopy given by

$$A = \frac{\hbar^2}{2I_a},\ B = \frac{\hbar^2}{2I_b},\ C = \frac{\hbar^2}{2I_c}, \quad A \geq B \geq C \tag{2.12}$$

2.2.2 Asymmetric rotor

In the general case of the asymmetric rotor all principal moments of inertia are different, $I_a \neq I_b \neq I_c \neq I_a$. The quantum number K as the projection onto the symmetry axis has no meaning anymore, because the rotor lacks a symmetry axis. If the molecule is near prolate or near oblate, however, the energy levels and wavefunctions should approach the ones of the corresponding symmetric case. To label the rotational states uniquely a pseudo-quantum number $\tau = K_- - K_+$ is introduced. K_- and K_+ are the projection of J onto the symmetry axis in the limiting case of the prolate and oblate symmetric molecule (see Fig. 2.2). To have a measure of the degree of asymmetry, it is convenient to define a asymmetry parameter κ by

$$\kappa = \frac{2B - A - C}{A - C} \tag{2.13}$$

In the limiting case of prolate symmetric rotor κ becomes -1, in the oblate case it is +1. Formaldehyde is near prolate ($\kappa = -0.97$) and behaves therefore similar to a symmetric prolate molecule (see Fig. 2.2). Finding eigenfunctions and eigenvalues (rotational energies) for the asymmetric rotor is non-trivial. For the calculation one needs to expand the searched eigenfunctions with an Ansatz into the eigenfunctions of the symmetric rotor. This Ansatz is put into the Schrödinger equation

$$H_{Rot}\,|\psi\rangle = E\,|\psi\rangle \tag{2.14}$$

with the rotational Hamiltonian (2.4). For solving the resulting equations we have to diagonalize for every J the matrix $\langle J, K|H_{Rot}\,|J, K'\rangle$. The obtained eigenvalues are the energy terms of the total angular momentum J. The convergence of the expansion in terms of symmetric rotor wavefunctions converges the faster the more the asymmetric rotor is near a limiting case (prolate or oblate). This is especially the case for formaldehyde which is near prolate (for details see [17]).

2.3 Vibrational motion

The vibrational motion of a nonrotating molecule is the movement of the nuclei with respect to the centre of mass of the molecule. Every general vibrational motion can be decomposed into a linear combination of several normal modes of vibration. A nonlinear molecule consisting of N nuclei has $3N$ degrees of freedom. Since 3 are translational and 3 are rotational, we are left with $3N - 6$ vibrational degrees of freedom. Those are called the normal modes of vibration. Every vibrational mode is characterized by its frequency ν_0 corresponding to the energy $h\nu_0$ of one vibrational excitation. This harmonic oscillator

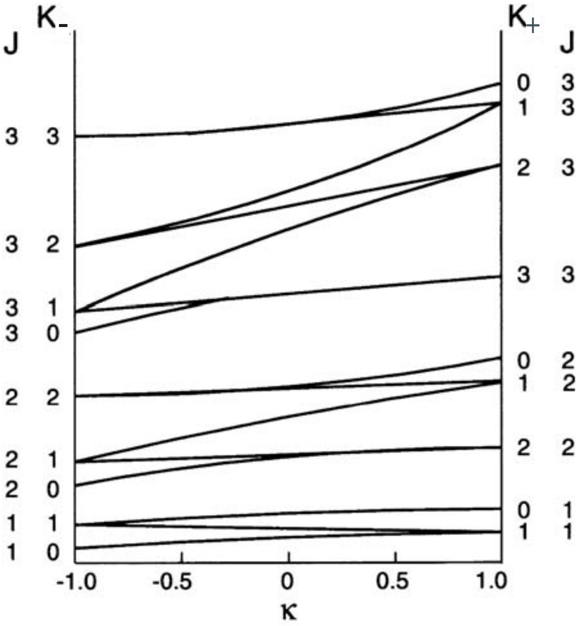

Figure 2.2: *Correlation diagram; shown is the rotational energy of different states of the asymmetric rotor for different asymmetry parameters κ. For the limiting case of $\kappa = -1$ ($\kappa = +1$) the energy levels are identical to the prolate (oblate) symmetric rotor (adapted from [17]).*

approximation holds only for low excitation of the normal mode (small displacements of the nuclei from their equilibrium position).

Formaldehyde is four-atomic and has therefore 6 normal modes of vibration (see Fig. 2.3). Important in this work is the out-of-plane bending mode ν_4 and the C-O stretch mode ν_2. They have been excited in the measurements of this work.

2.4 Non-rigid rotor

The rotation and vibration of a molecule has a influence on the moments of inertia. The effect of vibrational excitations are taken into account by averaging the rotational constants over one vibrational oscillation. The rotational constants are therefore different for every vibrational band. The rotational effect is included in the rotational Hamiltonian by correction terms that are expanded in terms of the rotational quantum numbers. The coefficients are not all independent, so that the Hamiltonian has to be transformed by an unitary transformation into a reduced form. Otherwise fitting of the coefficients to experimental data is not possible. It turns out that only even powers of J and K are needed (this is due to degeneracy of clockwise and anticlockwise rotation). The are $\mathrm{n}+1$ independent parameters for the n^{th} order of correction. The parameter set for slightly

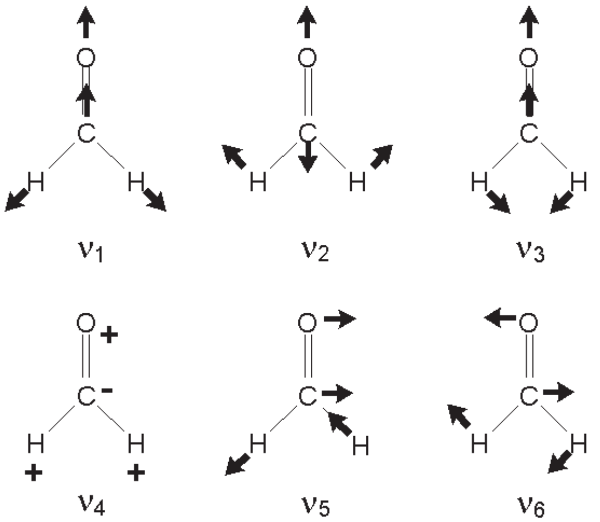

Figure 2.3: *All six vibrational normal modes of formaldehyde are shown. + and - means movement out of the molecular plane. The ν_4 out-of-plane bending and ν_2 C-O stretch mode are excited in the spectroscopy of this work*

order n	parameter
2	A, B, C
4	D_J, D_{JK}, D_K, d_J, d_K
6	H_J, H_{JK}, H_{KJ}, H_K, h_J, h_{JK}, h_K

Table 2.1: *Parameter set of reduced Hamiltonian in A-reduction.*

asymmetric molecules as formaldehyde is derived from the A-reduction Hamiltonian [18]. Its parameters up to sextic order are given in Table 2.1.

Chapter 3

Room-temperature absorption spectroscopy of formaldehyde

In this chapter results of the formaldehyde absorption spectroscopy are presented. As an introduction the necessity for doing conventional room-temperature absorption spectroscopy in this work is pointed out. Some basic facts about absorption spectroscopy are then described. After that the experimental setup, the measurements and the data analysis is shown. Finally the chapter concludes with presentation of improved molecular constants obtained from the measurements and calculated line positions that are used for the depletion measurements.

3.1 Introduction

The electrostatic quadrupole guide works well for molecules with a linear Stark shift. For the determination of the state distribution we have chosen formaldehyde, because its transitions to the first electronically excited state lie in the near UV. Most other simple molecules have electronic transitions in the deep UV region which is not so easily accessible by cw laser sources. An overview of the formaldehyde spectrum in the region of the electronical transition $\tilde{A}^1A_2 \leftarrow \tilde{X}^1A_1$ gives Fig. 3.1. The different vibrational bands can be seen. Every one of these vibrational bands has a substructure consisting of many rotational lines. To determine the rotational state distribution in our guide, the knowledge where the transition frequencies of the different rotational states within the chosen vibrational band lie is crucial. In the literature, however, no rotationally resolved spectrum of this region was found. The available molecular constants turned out to be too unprecise to calculate the transition frequencies correctly when compared to first measured spectra of a small range. Therefore room-temperature absorption spectroscopy was performed to get a line spectrum and to assign the lines correctly to the involved initial and final rotational states. For the depletion measurements we have chosen to examine the two strong vibrational bands $2^1_0 4^3_0$ and $2^2_0 4^1_0$ (see Fig. 3.1 for notation).

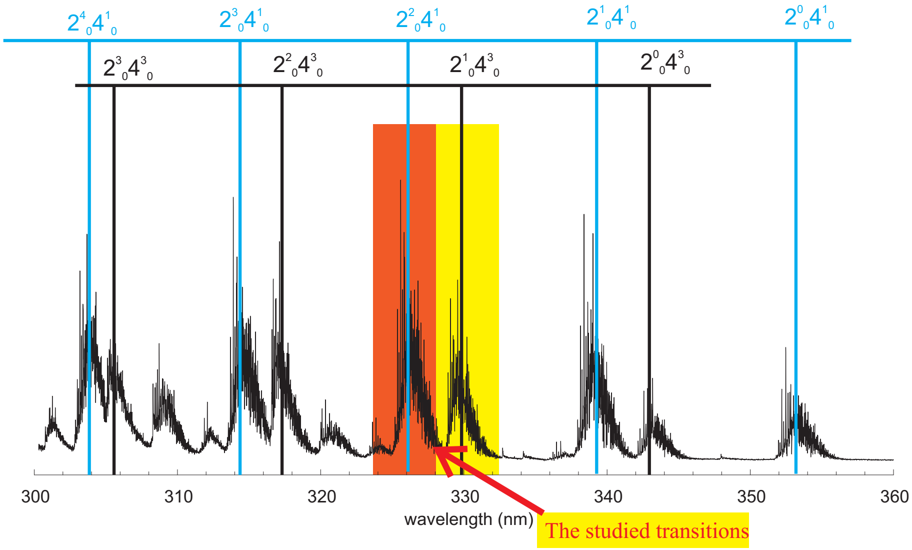

The studied transitions

Figure 3.1: *Overview of the vibrational bands of the electronic transition* $\tilde{A}^1A_2 \leftarrow \tilde{X}^1A_1$ *. The notations of the vibrational bands are* $\nu^{final}_{initial}\ \mu^{final}_{initial}$ *with* ν *and* μ *as the two different normal modes of vibration. The subscripts are the occupation numbers of the corresponding modes in the initial state, whereas the superscripts denote the occupation numbers in the excited state. The* ν_2 *mode corresponds to a C-O bond stretching and the* ν_4 *mode is the out-of-plane bending mode (see Fig. 2.3 for an overview of all modes). The rotational substructure is visible but not completely resolved. The studied transitions are in the red and yellow marked vibrational band (adapted from [19]).*

3.2 Absorption spectroscopy basics

The method of absorption spectroscopy is an established procedure to investigate molecular spectra. The principle of absorption spectroscopy [20] is described by the Lambert-Beer law

$$dI = -\alpha \cdot I \cdot dx \tag{3.1}$$

where dI is the change of intensity of the light by propagation through a dx long path in the absorbing substance. The absorption coefficient $\alpha(\omega)$ is given by

$$\alpha(\omega) = (N_i - (g_i/g_k)N_k)\sigma(\omega) \tag{3.2}$$

where N_i and N_k is the density of atoms or molecules in the initial state i and final state k with degeneracy factors g_i and g_k. The absorption cross section for the transition $i \rightarrow k$ is $\sigma(\omega)$. For small laser intensities N_i and N_k are not influenced strongly by the absorption

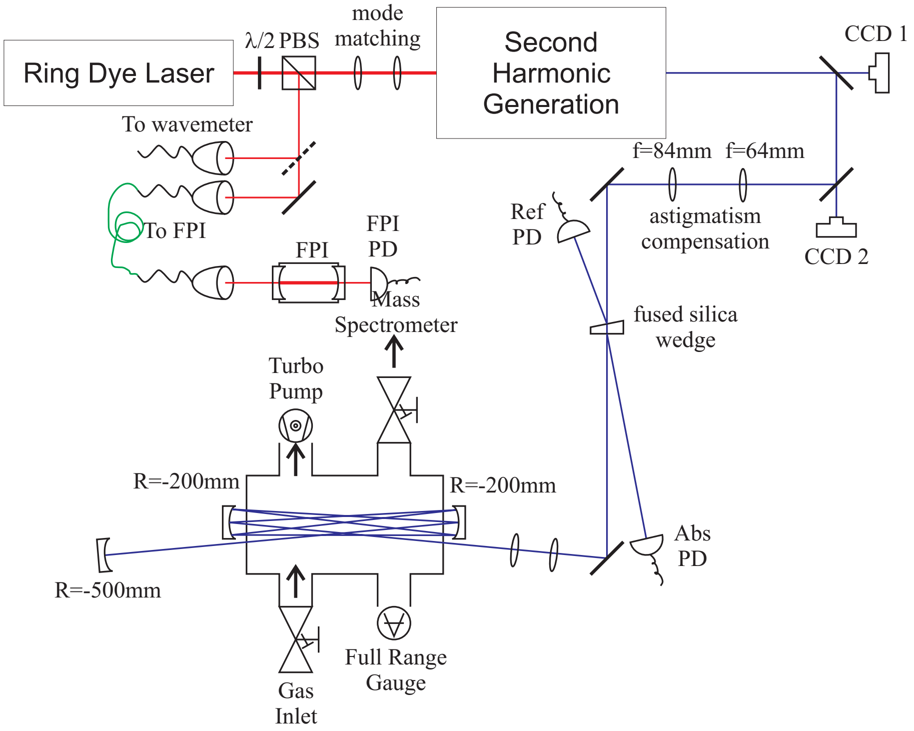

Figure 3.2: *Experimental setup of the absorption spectroscopy. Red light is produced by a dye laser and then frequency doubled into the UV range. A small fraction of red light is split off to a wavemeter and to a Fabry-Perot interferometer for frequency measurement. The absorption chamber is operated in a multipass setup. The transmitted and reference intensity is recorded by two photodiodes (Abs PD and Ref PD).*

since relaxation processes are much quicker and compensate for the absorption losses. In this case (3.1) can be integrated:

$$I(\omega) = I_0(\omega)e^{-\alpha(\omega)x} \tag{3.3}$$

where $I(\omega)$ is the transmitted intensity, $I_0(\omega)$ is the initial intensity, α is the absorption coefficient and x the absorption length [21]. The transmission is defined by

$$T \equiv \frac{I}{I_0} = e^{-\alpha(\omega)x} \quad . \tag{3.4}$$

3.3 Experimental setup

First the experimental setup is explained in detail. Doppler-free spectroscopy of formaldehyde was performed before with this setup [22], which is similar to most standard absorption spectroscopy setups [20]. Here an overview is given over the main ingredients for the measurements: UV laser light is brought into the spectroscopy chamber and the transmitted light intensity as well as a reference intensity without absorption is recorded as a function of frequency.

3.3.1 A more detailed description - The laser system

The studied transitions are in the range of 320–340 nm. Therefore a tunable narrow bandwidth UV light source is needed.
A ring dye laser (Coherent 899) is pumped by 10 W of a frequency doubled Nd:YVO4 at 532 nm, emitting red light at peak power of 1.3 W tunable between 600–670 nm. "DCM special" was chosen as dye for the laser. The laser is locked to an external temperature-stabilized reference cavity resulting in a linewidth of $\approx$ 0.5 MHz. This light is then frequency-doubled into the UV range by a cavity-enhanced Type II critical phase-matching (Coherent MBD-200) frequency doubler. The conversion efficiency of the frequency doubler is about 25 % leading to peak UV power of 350 mW. This high power is, however, not very stable due to thermal heating in the dye jet and in the crystal used for second harmonic generation. The power was reduced to about 100 mW for the measurements. Due to the Type II critical phasematching, the UV beam has a different divergence in horizontal and vertical direction (astigmatism), being compensated by a telescope of cylindrical lenses. Changing the frequency of the dye laser from scan to scan by changing the thick etalon, results in a small displacement of the beam (beam pointing), which was monitored in the residual transmission of two mirrors by two CCD cameras and manually realigned. In every measurement scan the frequency of the red light was swept over a range of 20 GHz. A small fraction of the red light is brought via fibers to a wavemeter (HighFinesse WS7) for frequency determination.

3.3.2 The spectroscopy chamber

The absorption spectroscopy was done in a vacuum chamber of 22.5 cm length. The optical absorption length was, however, increased by a factor of 14 to 3.15 m by using a multi-pass setup. This factor was achieved by placing two concave mirrors outside the chamber with a radius of curvature (RoC) of -200 mm, refocussing the light into the chamber. With the two mirrors the beam was made to pass the chamber seven times. By placing then a third mirror into the optical path the beam is retroreflected and passes the chamber another seven times. The detection of the measurement beam and the reference beam was achieved by placing a fused silica wedge into the optical path and focussing the reflected parts of the absorption and reference beams onto two Si photodiodes sensitive in the UV range (see Fig. 3.2).

The four vacuum chamber ports were connected to a turbo molecular pump, a pressure gauge (Pfeiffer Vacuum Compact Full Range Gauge PKR261), a flow valve for formaldehyde input and a flow valve leading to a quadrupole mass spectrometer (Pfeiffer Vacuum

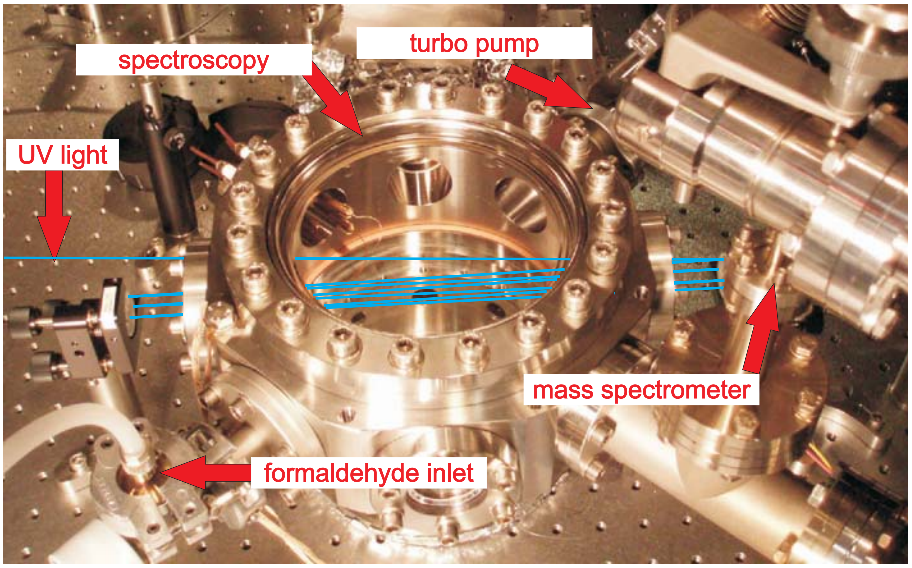

Figure 3.3: *Spectroscopy chamber with ports. The blue lines indicate the propagation of the laser light.*

Prisma QMS) enabling the analysis of the content of the spectroscopy chamber (see Fig. 3.3). With the turbo molecular pump we achieved a pressure of 10^{-6} mbar in the spectroscopy chamber when no formaldehyde was inside. Formaldehyde is produced by heating Paraformaldehyde (polymerized form of formaldehyde, from Sigma-Aldrich) to a temperature of 80–90 °C. To clean the dissociation products and remove unwanted water and polymer rests, the gas is lead through a dry ice cold trap at a temperature of $\approx$-80°C [23] before flowing it into the chamber via the inlet. Since formaldehyde molecules dissociate upon UV excitation, a stable flow of formaldehyde was maintained by slightly opening the valve between the turbo pump and the vacuum chamber. The ratio of formaldehyde and its dissociation products was monitored with the mass spectrometer and the formaldehyde input flow rate as well as the flow to the turbo molecular pump was optimized for a constant ratio. This way measurements could be performed at a constant formaldehyde concentration. Measurements were performed at a constant pressure of 0.5 mbar in the spectroscopy chamber.

3.4 Measurements

The measurements consisted of subsequent 20 GHz scans over the whole frequency range of the two vibrational bands. For every scan a voltage ramp was fed to the external scan input of the dye laser, causing the turn of the scanning brewster plate in the laser cavity. The scan width was limited to 20 GHz to ensure a mode-hop-free scan. The frequency-doubled light was then sent to the spectroscopy chamber. The silica wedge reflected a part of the UV light to the reference photodiode. The light which passed the spectroscopy chamber is also reflected by the wedge to the absorption photodiode. These two photodiode signals were recorded for every 20 GHz scan as a function of time.

Before and after every scan the wavelength measured by the wavemeter was annotated giving agreement within $0.001\,\mathrm{cm}^{-1}$ in the fundamental. Because the scanning speed of the dye laser is not constant, a further method was needed to determine the frequency while scanning. To translate the time signal of both photodiodes to the corresponding frequeny of the UV light at every time in the scan, an additional Fabry-Perot interferometer (FPI) was used. The transmission of the FPI was recorded by another photodiode, giving transmission maxima with a frequency distance of the FPI's free spectral range (FSR) of 1.0024 GHz (see Fig. 3.4). These are used as frequency marks. The scanning speed of the dye laser could then be determined by linear regression giving a typical value of $\approx 45\,\mathrm{GHz/s}$ (see Fig. 3.4). This was used for calibrating the scan speed for each individual scan.

The individual scans had a frequency difference of 10 GHz leading to an overlap between subsequent scans of 50%.

The data was recorded by a 4-channel digital oscilloscope (LeCroy WaveRunner 6050A) with the follwing channels:

- external ramp for the dye laser scan
- reference photodiode
- absorption photodiode
- FPI transmission photodiode

The sampling rate was 500 kS/s to have a good resolution for assigning the transmission peak maxima of the FPI. The individual traces were saved as files on the oscilloscope and the central frequency measured by the wavemeter was annotated.

3.5 Data analysis

The analysis consists of two steps: binning of data and finding FPI transmission peaks in a C program, then further analysis using a MATHEMATICA notebook.

3.5.1 C program

The C program written by M. Motsch and M. Zeppenfeld reads in the files by creating and filling four arrays, corresponding to the four channels of 500.000 data points with another array for the time stamp.
The FPI transmission peaks were found by analyzing channel 4. A voltage treshold of 30% of the maximum voltage of every trace has been set to find the FPI peaks and to distinguish

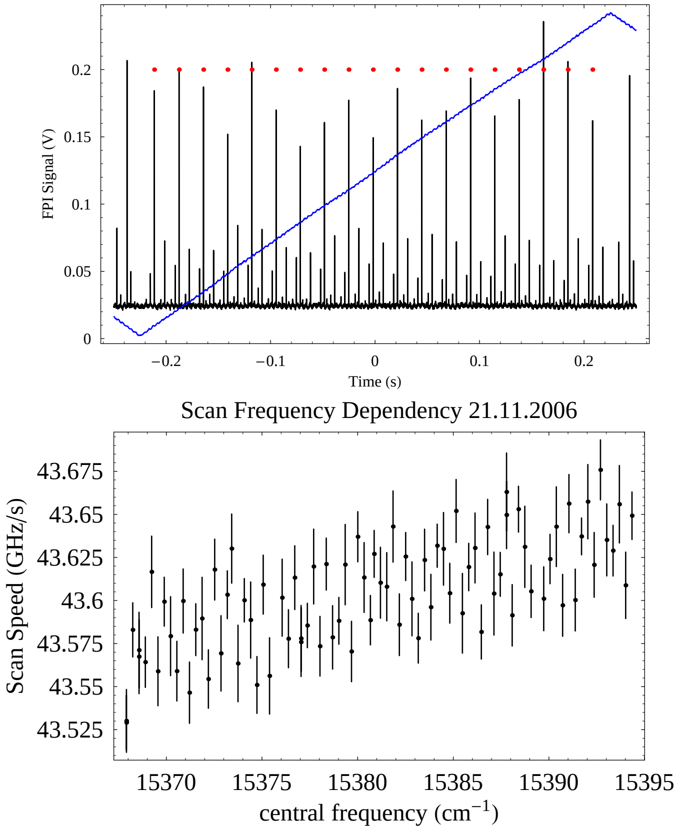

Figure 3.4: *top: The photodiode signal of the FPI transmission vs. time is shown while scanning the dye laser over 20 GHz (black). The ramp for the scanning brewster plate (blue) that causes the frequency change can be seen and the FPI peaks with their position in time (red dots). The smaller peaks correspond to higher-order modes of the FPI. bottom: Scanning speed over dye laser frequency; every data point represents one scan over 20 GHz of the dye laser as in the top picture. The slope of a linear fit of the FPI transmission peaks frequencies over time in the upper figure is used as scanning speed of the dye laser. The linear fit error is also indicated.*

between the main modes and the higher-order modes, which are roughly up to 10-20% of the ground modes signal (see Fig. 3.4). The maximum in every time interval, where the voltage is sufficiently high, is taken as the FPI transmission peak. The corresponding time of all the found peaks is saved as file. As next step the amount of data points is reduced by binning. The typical Doppler width at room-temperature is roughly 2 GHz. However, the data points were recorded with a frequency distance of 200 kHz. It is reasonable to increase the bin width to about 40-50 MHz. The binned data are written to file for further analysis.

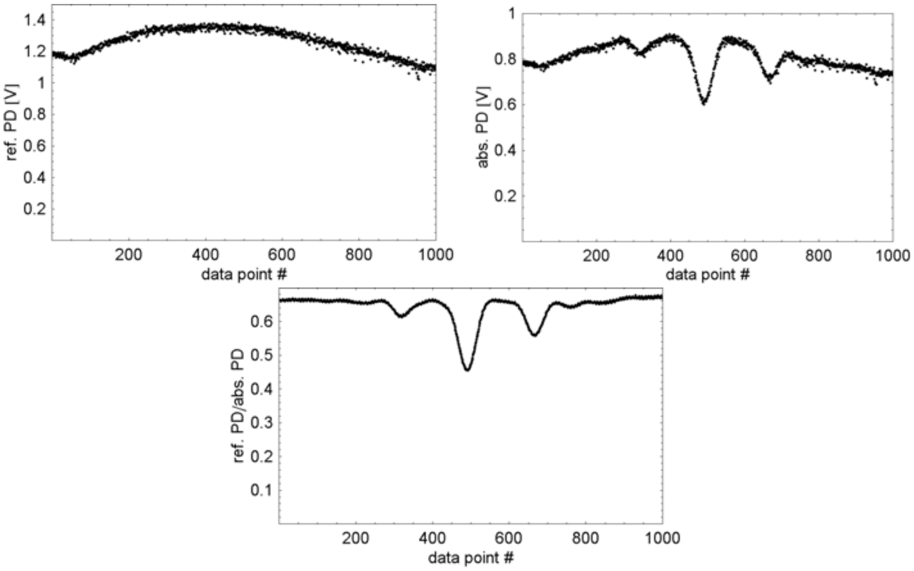

Figure 3.5: *Reference/absorption photodiode signal [V] versus datapoint number in a typical 20 GHz scan (left/right) and the divided not-normalized absorption spectrum (bottom).*

3.5.2 Further analysis

After reading in the binned data files, the transmission is calculated out of the photodiode (PD) signals (see eq. 3.4). Therefore the data of the absorption PD is divided by the reference PD for every measured time (see Fig. 3.5). This ratio is proportional to the transmission, but needs to be normalized in such a way that its equal to unity where no absorption is present. For each scan the maximum of the ratio is determined and the data of each scan is normalized to that maximum. This is finally the transmission.

The normalization procedure is valid under the assumption that every scan has a frequency where no absorption occurs, which is a reasonable for 40 GHz scan width in the UV light. Furthermore, at the turning point of the external ramp the error signal of the dye laser is bigger. The first and the last 75 points are therefore dropped. The normalized scans are now merged and overlapped to check if the frequency mapping worked (see Fig. 3.6). Lastly the joined spectrum of each of the two vibrational bands is binned to a bin width of about 250 MHz for the vibration bands.

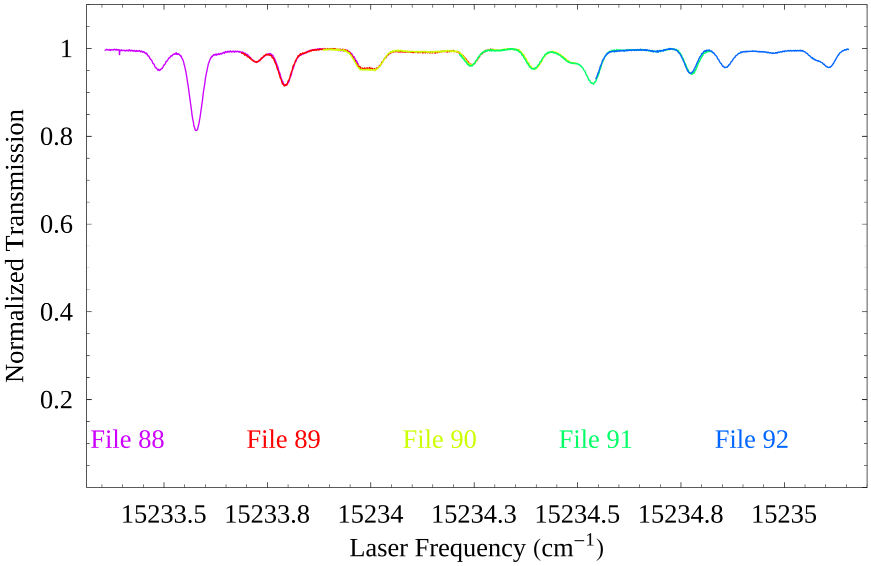

Figure 3.6: *Part of the concatenated spectrum to check overlap. Every colour represents one scan. Laser frequency is of the fundamental light.*

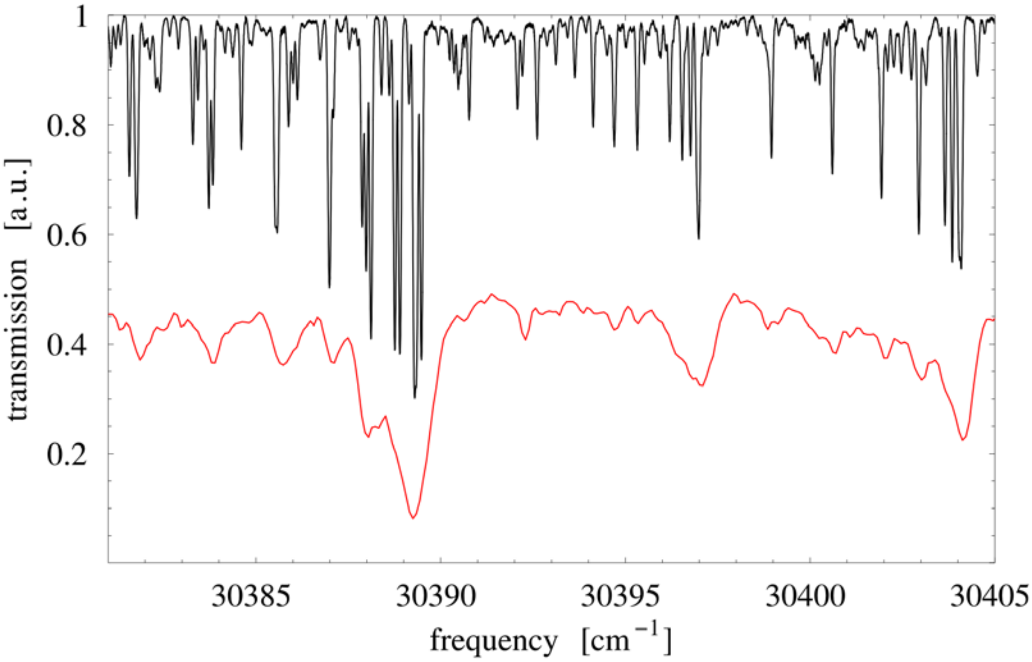

Figure 3.7: *Comparison in resolution of our data (black line, top) to previous measurements (red line, bottom). As an example the measurements by Smith et al. [24] with the so far highest reported resolution in this wavelength range are chosen as reference. The Smith et al. data is scaled to the range (0, 0.5).*

3.6 Results

The two vibrational bands $2_0^2\ 4_0^1$ and $2_0^1\ 4_0^3$ have been measured (see Fig. 3.1). The whole spectrum is depicted in the Appendix including the result of the spectrum fit (see Appendix A). By comparing the measurements with the formerly published formaldehyde spectra, a tremendous increase in resolution can be noticed (see Fig. 3.7 for comparison with Smith et al. [24]). It is now possible to recognize individual rotational lines in the spectrum.

To get improved rotational constants, a fit of both vibrational bands to the experimental data was performed. This was done in collaboration by PD Dr. Michael Schmitt from Düsseldorf. Watsons A-reduced Hamiltonian including quartic and sextic centrifugal distortion terms (see Table 2.1) has been used for the fit with a genetic algorithm as optimizer [25, 18]. This algorithm is based on the "survival of the fittest" principle as it is known in evolution theory. About 30 molecular constants as fit parameters were used. The fit procedure is described in more detail in Ref [26]. The result of this fit were refined molecule parameters. For the lower energy vibration band ($2_0^1 4_0^3$) the part above 30390 cm^{-1} of the spectrum was dropped to improve the fit parameters. This was necessary because the origin of the weak $2_0^2 4_0^3 6_0^1$ band is around 30395.00 cm^{-1} [27] and the fit simulated

$\vert J, K_-, K_+\rangle \rightarrow \vert J', K'_-, K'_+\rangle$	Frequency [cm^{-1}]
$\vert 1,1,0\rangle \rightarrow \vert 2,2,1\rangle$	30364.55
$\vert 2,2,0\rangle \rightarrow \vert 3,3,1\rangle$	30377.29
$\vert 3,3,0\rangle \rightarrow \vert 4,4,1\rangle$	30387.91
$\vert 4,3,1\rangle \rightarrow \vert 5,4,2\rangle$	30388.75
$\vert 5,3,2\rangle \rightarrow \vert 5,4,1\rangle$	30376.60
$\vert 5,5,0\rangle \rightarrow \vert 6,6,1\rangle$	30403.24

Table 3.1: *The transitions that were used later in the depletion measurement with the calculated transition frequencies (all from the* $2^1_0\,4^3_0$ *band). The states are labeled by* K_- *and* K_+*, the* K *quantum numbers of the projection of* J *on the figure axis in the limiting case of the prolate and oblate symmetric top.*

only one vibrational band. The underlying band made the fit worse without dropping. The resulting fit parameters for both of the measured bands are shown in table 3.2 and compared to the best previously published results. Especially the ground state rotational constants are in good agreement to the ones obtained by microwave spectroscopy [28]. The molecular constants of the excited states are improved compared to Ref. [24].

This enables us to calculate with these refined constants the line positions more precisely making the identification of lines in the depletion measurement much easier. An overview of the calculated transition frequencies that were used for the depletion measurements is given in table 3.1. Furthermore we can compare directly the absorption lines in the room-temperature measurements with the measurements in the electric guide, as will be done in chapter 5.

3.6.1 Possible improvements

The fit of the absorption spectrum shows quite good agreement with the measured spectrum. The main features are well reproduced by the fit. However, the intensities and positions for some lines mismatch. Therefore it is reasonable to ask what can be done better.

The pressure in the spectroscopy chamber was manually kept constant. Using a dose valve would result in more constant pressure conditions. Pressure changes are a relevant error source, since the absorption coefficient (3.1) depends on the molecular density. This could be an explanation for wrong fit intensities. The wavemeter was not calibrated every day , which could result in inaccuracies with changing temperature etc.. This error is estimated to be on the order of 0.001 cm^{-1} at the fundamental wavelength and is not a relevant error source. Nevertheless a seperate iodine absorption cell transmission signal can be used to indicate frequency inaccuracies.

Of course these error sources are on the experimental side, on the other hand the theory used for the genetic fit algorithm can be improved. The fit model already comprehends

the centrifugal distortion terms of quartic and sextic order. But the effects of coriolis coupling has been neglected. The vibrational modes 4 and 6 have similar eigenenergy and can therefore couple via Coriolis coupling. This is more eminent for higher quantum numbers J but has not been included in the model.
However, the refined constants turned out to be precisely enough for finding and identifying the transitions in the depletion spectroscopy.

Table 3.2: *Molecular parameters of the ground state (above, double-primed) and the* $\tilde{A}^1$ *excited state (below, primed) of formaldehyde from a GA-Fit of the* $2^1_0 4^3_0$ *and* $2^2_0 4^1_0$ *vibronic bands. All values are given in MHz. More details about the fit see text.* A, B, C *are the rotational constants.* D *and* d *are the quartic,* H *and* h *are the sextic centrifugal distortion terms. The* ν_0 *are the origins of the two vibrational bands.*

	GA-Fit $2^1_0 4^3_0$	GA-Fit $2^2_0 4^1_0$	Ref. [28]	
A”	281970.85(27)	281971.44(43)	281970.572(24)	-
B”	38836.53(27)	38836.14(25)	38836.0455(13)	-
C”	34002.67(16)	34002.57(25)	34002.2034(12)	-
10^3D_J”	75.38(7)	75.61(11)	75.295(21)	-
10^3D_{JK}”	1290.24(20)	1290.00(29)	1290.50(37)	-
10^3D_K”	19424 (1)	19424.1(7)	19423(7)	-
10^3d_J”	9.85(24)	10.30(25)	10.4567(9)	-
10^3d_K”	1028.39(60)	1027.68(66)	1026.03(25)	-
10^6H_J”	0.0335(16)	0.0341(19)	0.031(21)	-
10^6H_{JK}”	29.021(110)	29.022(12)	29.019(690)	-
10^6H_{KJ}”	-112.183(28)	-112.179(32)	-112.180(280)	-
10^6H_K”	4469(251)	4469(412)	4499(200)	-
10^6h_J”	0.045(13)	0.040(9)	0.0423(17)	-
10^6h_{JK}”	15.6(5)	15.6(6)	15.7(3)	-
			$2^1_0 4^3_0$Ref.[24]	$2^2_0 4^1_0$Ref.[24]
ν_0	909572633(41)	919120592(48)	909571763(1110)	919120745(690)
A'	246402.7(48)	259111.5(43)	246669(90)	259090(21)
B'	33158.0(32)	32952.3(32)	33194(21)	32918(16)
C'	30268.8(28)	29764.3(39)	30277(21)	29837(14)
$10^3D'_J$	145.9(44)	89.6(9)	188(17)	99(12)
$10^3D'_{JK}$	3204(51)	1616(14)	4886(450)	1484(45)
$10^3D'_K$	-43023(62)	9473(98)	-48237(1919)	9383(33)
$10^3d'_J$	-9.8(40)	23.0(23)	49(14)	10(12)
$10^3d'_K$	16353(695)	189(384)	11892(4497)	-6175(959)
$10^6H'_J$	6.48(9.97)	0.016(18)	-	-
$10^6H'_{JK}$	-20(12)	30(5)	-	-
$10^6H'_{KJ}$	154(80)	158(88)	-	-
$10^6H'_K$	8767(618)	3244(643)	-	-
$10^6h'_J$	-24(8)	0.051(12)	-	-
$10^6h'_{JK}$	28(2)	14(6)	-	-
$10^6h'_K$	3134(491)	1485(107)	-	-

Chapter 4

State-selective detection via depletion spectroscopy

The main topic of this work is the measurement of the rotational-state distribution of a velocity-filtered guided beam of cold polar molecules.

In the first section this filter (from now on called "guide" for reasons becoming clear in the next section) will be described with its experimental realization. In the second section experiments and theoretical descriptions are reviewed that have already been performed with it. The following third section describes the idea to determine the rotational-state distribution of the guided molecules. A theoretical model for the expected data is developed. The concluding section is about the experimental setup and the alignment for the measurements, which are presented in the next chapter.

4.1 Electrostatic quadrupole guide as a velocity filter

4.1.1 Idea

The electrostatic quadrupole guide acting as a velocity filter has been already described in detail elsewhere [29, 30].

Its principle of operation and its most relevant characteristics will be reviewed in this section. The central idea of the slow molecule source is to use the fact that in a room-temperature thermal molecular gas a small fraction of slow molecules is already present. One only needs to filter them out efficiently. The guide designed at MPQ in the group of Prof. Rempe works as follows.

Molecules in the gas phase are coming out of an effusive thermal source and are injected into the field minimum of an electrostatic quadrupole field. Molecules that are in a rota-

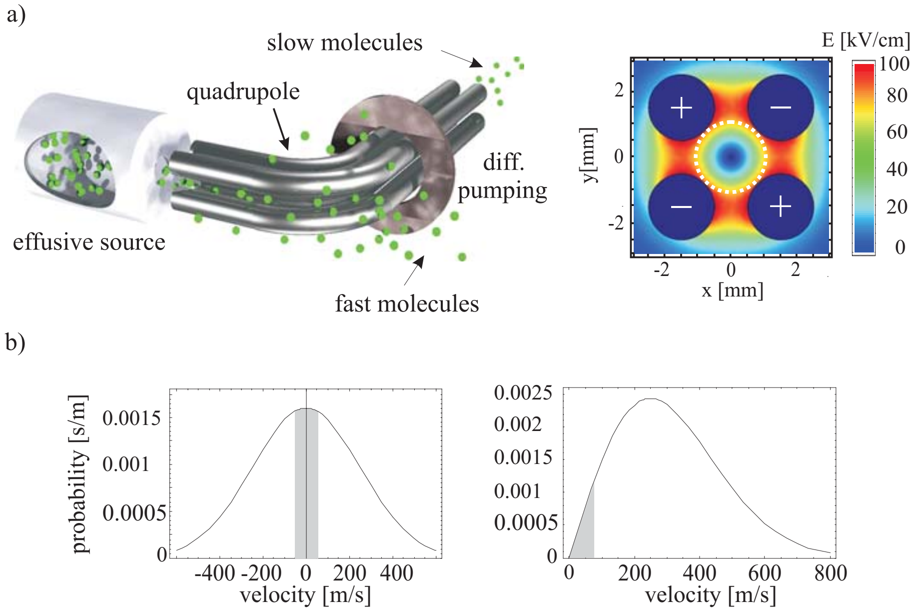

Figure 4.1: *(a) Schematic sketch which illustrates how slow polar molecules are filtered from a thermal gas. Molecules from an effusive source are injected into a bent electrostatic quadrupole with a free inner radius r indicated by the dashed circle in the field plot. Only transversely slow molecules which cannot overcome the Stark potential barrier are kept within the guide, whereas longitudinal velocity selection is provided by the bend. (b) Guided fractions are displayed as shaded regions in the transverse (left) and longitudinal (right) velocity distribution of the gas (e.g.* ND_3 *and* $T = 300K$*)[30].*

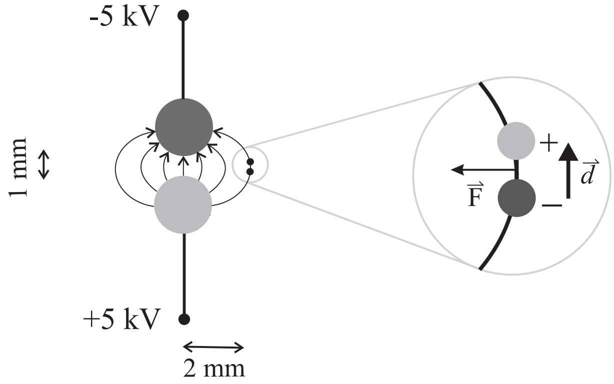

Figure 4.2: *Classical dipole in an inhomogeneous electric field generated by two cylindrical electrodes. When the dipole moment is oriented parallel (antiparallel) to the electric field lines, the dipole experiences a net force towards higher (lower) electric fields [30].*

tional state which has a positive Stark shift (so they increase their internal energy with increasing electric field strength) see this electric field as a repulsive potential. If their transverse kinetic energy is too high, they can overcome this potential and escape. If their velocity is small enough, they will be trapped in two dimensions in this electric field. Their longitudinal velocity is not affected. To filter also on the longitudinal velocity, the guide is bent. Molecules that are longitudinally too fast cannot follow the bend and are lost as the centripetal force exerted by the Stark shift is too small. Clearly only molecules with a positive Stark shift (i.e. so called "low-field seekers") are guided in this filter, the others are lost (see Fig. 4.1).

The dependence of the Stark shift on the rotational state of the molecule can be explained in an intuitive picture. Depending on the time-averaged orientation of the dipole moment of the molecule with respect to the electric field, we find a low-field seeking state if the averaged dipole moment is antiparallel to the electric field, and high-field seeking state for parallel orientation (see Fig. 4.2 for the classical picture). This effective dipole moment as time average leads to the state-dependent Stark shift. To calculate the effect of the electric field on the different rotational state energies quantitatively, one has to do numerical calculations. This was done by M. Motsch using a C program diagonalizing the Hamiltonian for the asymmetric rotor for the different electric field strengths. This follows mainly the recipe in the paper by Hain [31].

4.1.2 Experimental implementation

The experimental setup of the quadrupole guide is shown in Figure 4.3. The formaldehyde gas is produced by heating paraformaldehyde and leading it through a dry ice cold trap as already described in the room-temperature spectroscopy chapter (3.3.2). The molecules are brought to the guide by a gas inlet capillary of Teflon. To increase the fraction of slow molecules in the thermal gas, it is cooled. For this purpose the capillary which carries the molecules is wound in a meander-like way of 8 cm length through a copper block as thermalisation body, which is thermally linked to the liquid nitrogen reservoir. Inside the copper block the molecular gas thermalizes to the ambient temperature. To be able to increase the temperature also to higher values a thermo coaxial heater cable was wound inside the copper block. The temperature of the molecules can be changed with our parameters in a range of 100–400 K.

At the end of the Teflon tube a 1.5 mm diameter ceramic nozzle is mounted which injects the molecules into the quadrupole, whcih consists of four rods with a total length of 60 cm. The guide is led through three vacuum cubes connected through two differential pumping stages. In the first cube most of the molecules are lost and need to be pumped away quickly. Using a turbomolecular pump with a pumping speed of 500 l/s, a pressure of 10^{-7} mbar is maintained. The guide is brought by a bend (radius of curvature 50 mm) to the second cube. Combining the already mentioned differential pumping stage

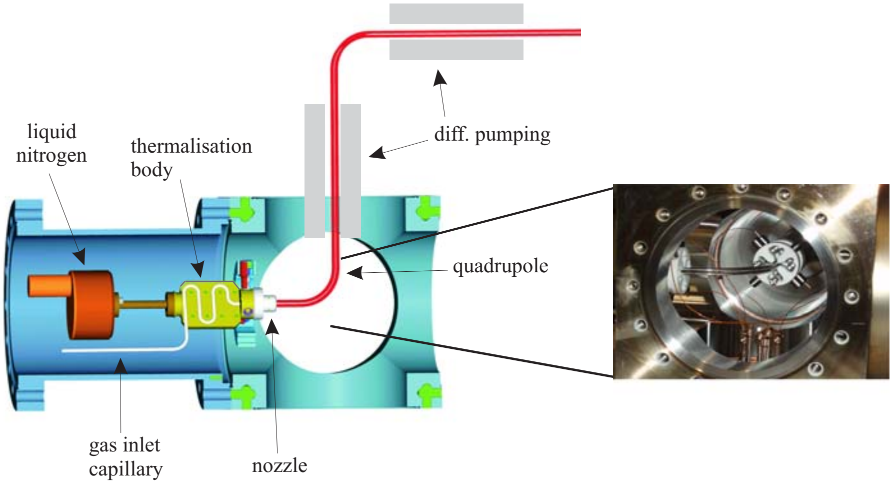

Figure 4.3: *Cut through the gas inlet chamber of the experimental setup. The liquid nitrogen cooling stage with the connected gas inlet system and the quadrupole is shown. Gas enters the chamber in a thin flexible Teflon tube which passes through a copper block before it ends in the exit nozzle. The copper block with the nozzle assembly is connected to the liquid nitrogen reservoir via a thermal link and heating elements allow nozzle temperature variations from 100 K to 400 K. The inset is a view into the opened first chamber of the guide. The first bent segment is clearly visible (adapted from [30]).*

with a pump of 250 l/s pumping speed, this leads to a pressure of few times 10^{-9} mbar. Another bend finally leads the guide through the second differential pumping stage into the last cube, the QMS detection region. The pressure in the UHV vacuum chamber of the mass spectrometer region is about 10^{-11} mbar. This low pressure is necessary to have a low background countrate in the mass-spectrometer signal. The mass spectrometer is an ionizing quadrupole mass spectrometer (QMS, Pfeiffer Vacuum QMG422) in cross beam configuration. The efficiency of the mass spectrometer is on the order of 10^{-4} counts/molecule.

4.2 Known experiments and theory of the guide

To point out what experiments have been already performed with the electric guide, it will be reviewed briefly. Also a theoretical description of the filtering process will be given. More details can be found at [30, 32, 29].

4.2.1 Longitudinal and transverse velocity distribution

The molecules are injected into the quadrupole field from a effusive source. A source is effusive if the mean free path of the molecules is bigger than the dimensions of the exit hole. Essentially this means that the velocity distribution of molecules leaving the source is the same as inside the source. Leaving the effusive regime by increasing pressure leads to collisions of molecules with each other at the exit hole and the slow molecules are accelerated to higher velocities which is not aspired since we want to filter the slow molecules. For transversely slow molecules with a positive Stark shift is the quadrupole field a conservative trapping potential. In the following is the z-axis in longitudinal direction of the guide axis, x- and y-axis are orthogonal and in the transverse direction.

For the transverse velocity distribution in the guide of one molecular state we yield from the Maxwell-Boltzmann distribution

$$P(v_\rho) = \frac{1}{\alpha\sqrt{\pi}}\ e^{-v_\rho^2/\alpha^2} \ \ (|v_\rho| < |v_{max}|) \quad , \tag{4.1}$$

with the most probable velocity in the gas $\alpha{=}\sqrt{2k_BT/m}$ (k_B is the Boltzmann constant and m the molecular mass), the transverse velocity $v_\rho = \sqrt{v_x^2 + v_y^2}$ and the maximum transverse velocity v_{max}. The maximum transverse velocity depends on the depth of the potential, given by the Stark shift of the molecule, by the applied guide voltage and by the injection point. For a given Stark shift $W^S(E)$ and injection at zero electric field we get the maximal transverse velocity that can still be trapped:

$$v_{max} = \sqrt{\frac{2W^S(E_{max})}{m}} \quad , \tag{4.2}$$

with $W^S(E_{max})$ as the Stark energy at maximum trapping electric field strength.

The longitudinal velocity distribution is not yet filtered and is given by the molecules in the reservoir passing through a plane with velocity component v_z perpendicular to the plane:

$$P(v_z) = \frac{2v_z}{\alpha^2}\ e^{-v_z^2/\alpha^2}. \tag{4.3}$$

Longitudinal filtering is provided by a bent segment of the quadrupole guide. The molecules with a given longitudinal velocity are guided around the bend if the corresponding centrifugal force at the bend is smaller or equal to the force brought up by the electric field. If we assume a radially linear rising electric field (quadrupole field) we get for maximal longitudinal velocity:

$$v_{lmax} = \sqrt{\frac{W^S(E_{max})}{m}\frac{R}{r_0}} = v_{max}\sqrt{\frac{R}{2r_0}} \quad , \tag{4.4}$$

v_{lmax} is the longitudinal cut-off velocity, R is the radius of curvature of the bend and r_0 is the open inner radius of the quadrupole guide (see white dashed line in Fig. 4.1a) right).

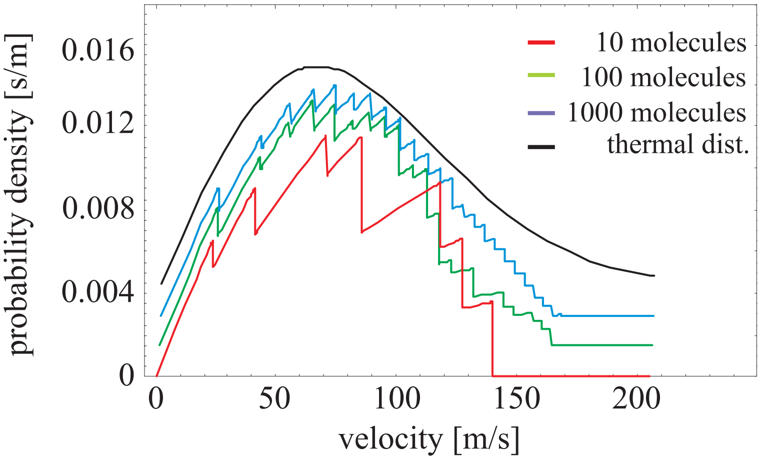

Figure 4.4: *Longitudinal velocity distributions after filtering are shown for 10, 100 and 1000 molecules with randomly chosen molecular Stark shifts out of 25 possible shifts. It is obvious that the velocity distribution shows sharp discrete structures indicating the velocity cutoffs for the particular molecular states. For 1000 molecules, it can be seen that the discrete structures are smoothed and the velocity distribution can be described by a one-dimensional thermal distribution. The remaining structure in the distribution stems from the underlying discrete state distribution used in this example. Note that the different distributions are shifted for a better visibility (Fig. from [30]).*

The longitudinal velocity distribution can be experimentally obtained by analyzing the mass spectrometer signal when the quadrupole field is switched on. The molecules with highest longitudinal velocity contribute early and the slower ones later to the signal. The velocity distribution can be derived from the slope of the signal.

In the thermal source molecules occupy many different rotational states with different Stark shifts leading to different longitudinal cut-off velocities. The total longitudinal velocity distribution will be a distribution integrated over all contributing molecular states (see Fig. 4.4). With the depletion method it will be possible to measure the velocity distribution of one rotational state, as shown in 5.3.

4.2.2 Experiments with the guide - State of the art

Guiding of various molecules has been achieved hitherto, for example ammonia (ND_3), formaldehyde (H_2CO) and heavy water (D_2O) [33]. Even guiding of molecules in high-field-seeking rotational states is possible by use of time-varying electric fields [34]. The quadrupole guide was used as a cold molecule delivery tool for loading an electrostatic trap for ammonia molecules, where trapping times of 130 ms and a trap depth of 300 mK was achieved [35].

4.3 Depletion idea and theoretical expectations

Molecules are expected to contribute to the molecular flux depending on their Stark shift at the trapping electric field and their thermal occupation in the source of the thermal gas [33]. The way to examine this distribution is to address the guided rotational states by inducing a transition to an electronically excited state. The molecules in the excited states typically decay with a lifetime of the order of 10 ns into a vibrational highly excited electronic ground state and dissociate then [36]. This leads to a loss in the guided flux.

There are many different rotational states contributing to the total flux of molecules inside the guide. As a practical compromise only the six rotational states $|J, \tau\rangle$ with the highest expected population were examined in this work. Those states make up about 30% of the total molecular flux.

Using the refined molecular constants achieved with the room-temperature measurements, we can calculate the line positions of transitions from the selected guided states (see chapter 3.6 Table 3.1). Setting the UV laser to the frequency of a transition from a guided state, the loss in guided flux compared to a measurement with laser light being switched off is recorded.

For each state the measurements were done basically in two steps. First the laser frequency was scanned over the calculated transition frequency of the state. This measured the line shape of the QMS (quadrupole mass spectrometer) loss signal. The dependence of the peak maximum on the UV power was measured, to see what loss signal is reached in the limit of high laser power. Assuming that every molecular trajectory leads through a field region that is overlapped with the resonant laser field, each molecular state could be completely depleted. As there might be a small fraction of trajectories that do not pass through the resonant laser beam region, this estimate is a lower limit for the population of this state.

The measurement results are shown later on (chapter 5), first a theoretical model will be developed in the next three subsections for the expected rotational state distribution, the line shape and the UV power dependency.

4.3.1 Expected rotational state distribution

We can restrict ourself to the rotational state distribution, omitting any molecular states that are also vibrational excited. To justify this approximation, one has to consider the vibrational energies of the normal modes of the molecule. For formaldehyde the vibrational mode with lowest energy is the ν_4 out-of-plane-bending mode with an energy $E_{v_4} = 1167$ cm$^{-1} \cong 1600$ K [28]. The number of molecules in that and higher states can therefore be neglected at room-temperature.

The rotational state distribution of the guided molecules is determined by two factors: the thermal occupation of the states in the thermal gas reservoir and how efficiently they are guided, which depends on the trap depth and therefore on their Stark shift.

In a thermal gas, the dominant factor governing the population of a state is the the Boltzmann-factor. For a rotational state $|J, K_{-1}, K_{+1}\rangle$ with rotational energy W_{rot} in a thermal gas at temperature T we get for the normalized population probability

$$p_{source}(J, K_{-1}, K_{+1}) = \frac{1}{Z_{source}} e^{-W_{rot}/(k_B T)} g_M g_{NS} \qquad , \tag{4.5}$$

with $1/Z_{source}$ as normalization factor, $g_M = (2J+1)$ expresses the M degeneracy of the rotational state if no electric field is present, g_{NS} is the nuclear spin degeneracy. The spin degeneracy is 3 or 1 for formaldehyde depending on the parity of the rotational state. This follows from the necessity that the overall wavefunction is antisymmetric.

Because the flux depends quadratically on the Stark shift W_{Stark} of a state at the trapping electric field, we need to weigh the source state distribution (4.5) with the squared Stark shift at the electric field strength of the trapping field. The (2J+1)-fold degeneracy is lifted by the electric field. The population of states after the Stark filter is then given by

$$p(J, K_{-1}, K_{+1}, M) = \frac{1}{Z_{guide}} e^{-W_{rot}/(k_B T)} g_{NS} W_{Stark}^2 \qquad . \tag{4.6}$$

This population is now also dependent on the quantum number M, the projection of J onto the electric field axis. Again there is a normalization factor of $1/Z_{guide}$. Z_{guide} is yielded by

$$Z_{guide} = \sum_{J,\tau,M} e^{-W_{rot}/(k_B T)} g_{NS} W_{Stark}^2$$

This is an infinite sum, summing over all states, but in the calculation the summing has been limited to $J_{max} = 30$ representing a minimum rotational energy of $W_{rot}(J = 30, \tau = -30) = 187\text{cm}^{-1} \cong 1500\,\text{K}$. The population of the states with $J > 30$ can be neglected at the temperatures at which we measured. Table 4.1 shows the most contributing states in the molecular beam.

4.3.2 Theoretical model of line shapes

What effects are important for the line position, shape and strength of the measured signals? The following effects have to be taken into account

1. Zero-electric-field frequency of the transition
2. Natural linewidth
3. Doppler broadening and shift (resulting from longitudinal velocity distribution)
4. (non-)saturation effects

Rotational State $\vert J,\tau,M\rangle$	W_S (cm^{-1}) @100 kV/cm	Source Pop. (%) @150 K	Guided Pop. (%) @100 kV/cm
$\vert 3,3,3\rangle$	2.86	0.252	8.52
$\vert 4,2,4\rangle$	2.28	0.230	4.93
$\vert 1,1,1\rangle$	1.29	0.531	3.62
$\vert 3,3,2\rangle$	1.82	0.252	3.46
$\vert 2,2,2\rangle$	2.42	0.134	3.22
$\vert 5,1,5\rangle$	1.90	0.205	3.05

Table 4.1: *Calculated Stark shifts W_s and population of selected rotational states $|J,\tau,M\rangle$ in the source and in the guide. Note the increase of population of these states relative to their contribution in the source by a factor of 10 to 35.*

5. Stark shifts due to the electric fields in the guide

The frequency where most loss of an guided state is found is of course near the zero-field frequency ν_0 of the considered transition. The last four effects (2.-5.) influence the shape of the depletion signal. The natural linewidth of the transitions is determined by the lifetime of the excited state. As shown by [22] the typical linewidth is on the order of 50 MHz. Because the UV light is counterpropagating to the molecules, the resonance frequency is Doppler-shifted to the red. At a voltage of the electrodes of 1 kV this leads to v_{lmax} =100 m/s and hence a maximum Doppler shift of ν_{dopp} =300 MHz. The line shape will be also influenced by the power of the UV light by saturation, similar to the classical absorption spectroscopy. But the main effect influencing the line shape is a result of the Stark shifts of the initial and final state of the transition. While the molecules fly through the guide, their trajectories probe electric fields ranging between 0 kV/cm and 85 kV/cm at 5 kV guide voltage. All the examined transitions have a negative differential Stark shift of at least -1 $\mathrm{cm}^{-1}/(100\,\mathrm{kV/cm})$ which translates into frequency shifts up to 25 GHz to lower energies with respect to ν_0. This will be the dominating effect for the line shape.

Shining in laser light with a defined frequency $\nu \leq \nu_0$ will only cause transitions in a small spatial region where the electric fields shift the transition frequency via the negative differential Stark shift from the zero-field frequency ν_0 to the frequency of the laser light. The electric field is independent on the longitudinal position in the guide (neglecting the electrodes beginning and end) and linearly rising in the transverse direction (see Fig. 4.5b)) Therefore for a given frequency $\nu \leq \nu_0$ we have a small ring in the transverse plane, where the electric field strength shifts the transition frequency from ν_0 to ν (see Fig. 4.5a)).

The width of the ring dr is given by the electric field gradient (resulting from the applied guide voltage), the differential Stark-shift between the initial and final state and the natural linewidth of the transition. A higher absolute differential Stark-shift, a higher guide voltage and a smaller linewidth decreases the ring width.
The loss of molecules as function of frequency shall be proportional to the number of

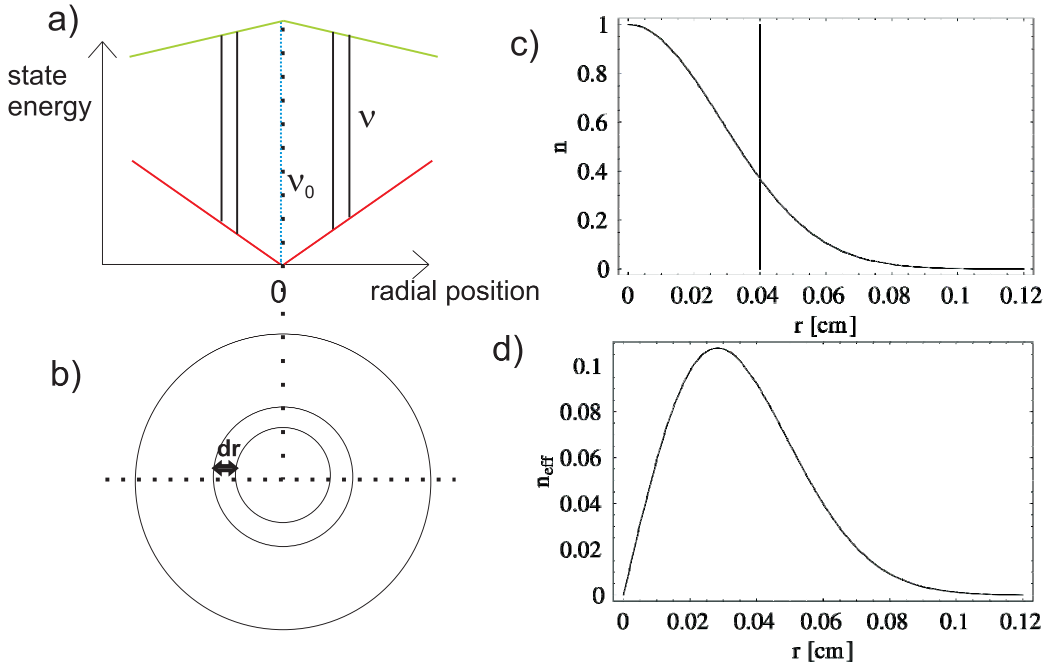

Figure 4.5: *a) Radial position dependent state energy and transition frequency* ν *for two typical involved states (red: initial state, green: final state). Upper state is high-field seeker and lower state is low-field seeker. The zero-field transition frequency is* ν_0*. b) Cross section of the guide. Inside the biggest circle are the molecules distributed. The smaller two concentric circles represent the ring in which molecules can be addressed for a given Stark-shifted transition frequency* ν*. c) Molecular radial distribution* $n(r)$ *as Gaussian with width* $r_0 = 400\,\mu m$ *indicated by vertical line. d) Molecular number density* $n_{eff}(r) = 2\pi r n(r)$ *for a ring with radius r.*

molecules whose transition frequency coincides with the laser frequency within the natural lineshape.

A formula for the depletion signal is obtained by integrating the radial dependent transition frequencies over the radial molecular distribution. This is weighted furthermore with the radial dependent light intensity. The depletion signal Δ is

$$\Delta(\nu) \propto \int_0^{r_{max}} dr n_{eff}(r) \cdot g_{\nu_0}(\nu + \Delta\nu(r)) \cdot I_{UV}(r) \quad , \tag{4.7}$$

with $n_{eff}(r) = 2\pi r\ n(r)$ as the density of molecule in a ring with radius r (see Fig. 4.5 d)), $n(r)$ as the radial distribution of molecules in the guide (see Fig. 4.5 c)). $g_{\nu_0}(\nu)$ is the natural line shape of the transition with resonance at ν_0, $\Delta\nu(r)$ is the frequency shift induced by the electric field strength at radial position r and $I_{UV}(r)$ the laser intensity at position r.

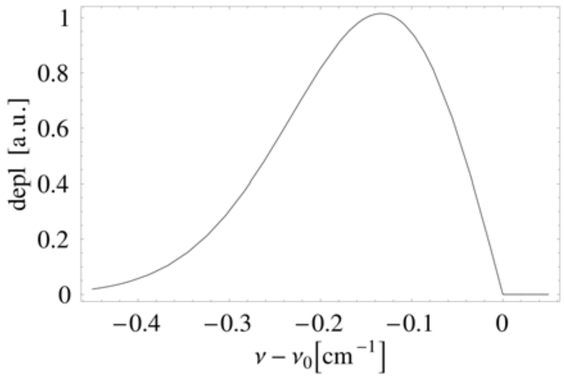

Figure 4.6: *Plot of the function (4.8) to show the predicted asymmetric line shape. Zero-field-frequency is set to 0 (Parameters: UV waist* $\omega_0 = 200\,\mu m$*, molecule radial distribution* $r_0 = 400\,\mu m$*, guide voltage* $U_{guide} = 5kV$*,* $r_{max} = 1.2\,mm$ *and differential Stark shift of* $0.01cm^{-1}/(1kV/cm)$*)*

Approximating the laser intensity distribution by a Gaussian beam with a constant width ω_0 and assuming a Gaussian distribution of the molecules with width r_0, we get for the depletion signal:

$$\Delta(\nu) = \alpha \int_0^{r_{max}} 2\pi r dr\ n(r) \cdot g(\nu + \Delta\nu(r)) \cdot \exp(-2(r/\omega_0)^2) \quad , \tag{4.8}$$

$$n(r) = n_0 \cdot \exp(-(r/(r_0)^2) \qquad ,$$

$$\Delta\nu(r) = \frac{\Delta W^S E(r)}{h} \qquad ,$$

with α a proportionality constant, $\Delta W^S = W^S_{final} - W^S_{initial}$ as the differential Stark shift between the transitions, $E(r)$ the electric field strength at radial position r and h Planck's constant. Three free parameters are used for the fit: α reflects the efficiency of addressing tha molecular state, ν_0 is the zero-field transition frequency and ΔW^S is the differential Stark shift between the states (in units of $\mathrm{cm}^{-1}/(1\mathrm{kV/cm})$).

4.3.3 Theoretical model of power dependency

The essential question to be answered in this work is: what rotational state population is provided by the quadrupole guide. To get this fraction for the biggest contributing states we looked at the depletion signal at the frequency of the peak maximum and varyied the UV power. To get a fit function for the power dependency, a model is derived in this subsection.

For this we assume shining a laser with power P collinearly with the molecular beam in the guide. The frequency of the laser is chosen to be on the maximum of the lineshape of a transition. The loss of molecules in the guided initial state that are addressed with the laser shall be $dN = -N\,P\,\alpha\,dt$ with N as number of molecules in that state, P the UV power, dt the considered time interval and α a proportional constant that is dependent on the overlap with addressable molecules. Out of this we get the usual exponential

$$N_P(t) = N_0 e^{-\alpha P t} \qquad , \tag{4.9}$$

as the number of molecules that "survived" the laser beam of power P and did not get dissociated up to a time t $[N_0 = N(t = 0)]$. The important fact now is that the interaction time $t_{int} = l/v$ is velocity dependent (l is the interaction length). The slow molecules are dissociated more easily due to longer interaction time. Therefore we have to integrate over the longitudinal velocity distribution. For the number of molecules that are still in the guided state after interaction time $t_{int} = l/v$ now as a function of laser power this results in:

$$N(P) = \int_0^\infty dv\, n(v) e^{-\alpha P l/v} \tag{4.10}$$

For $n(v)$ the longitudinal velocity distribution for one state is used in the linear approximation (see eq. 4.4). That holds for molecules that are slow compared to the most probable velocity α in the Boltzmann distribution. The distribution is

$$n(v) = kvH(v)H(v_{max} - v) \quad , \tag{4.11}$$

with the Heaviside step function ensuring positive velocities below v_{max} and k as normalizing constant. Out of $N(P)$ we get for the fraction of dissociated molecules compared to the overall number of molecules N^0 in this state $\Delta = \frac{N^0 - N}{N^0} = (1 - \frac{N}{N^0})$ with $N^0 = \int_0^\infty n(v)dv$. The actually measured signal is the loss of molecules compared to the overall flux of all the various rotational states. Therefore the depletion signal becomes

$$\Delta(P) = p_0 \left(1 - \frac{N(P)}{N^0}\right) \quad , \tag{4.12}$$

with p_0 the population of this state. This function has been used as fit function of the measured power dependencies to get p_0 as fit parameter of the states population. The results of the fit will be shown in the next chapter.

4.4 Depletion setup

The UV light is provided by the same configuration as described in the room-temperature spectroscopy chapter, i.e. essentially a frequency-doubled cw narrow bandwidth dye laser.

To compare the flux of molecules with laser light inducing a transition to the absence of laser light, it is necessary to switch the UV beam. This was achieved with an electro-optical

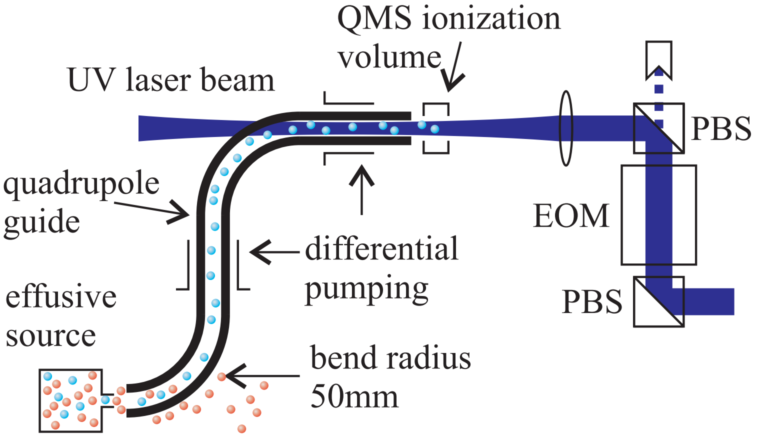

Figure 4.7: *Setup of the depletion experiment*

modulator (EOM) that rotates the polarization of the incoming beam by 90 degrees when adequate voltage is applied to it. It is combined with two polarizing beamsplitter (PBS), one before the EOM to have pure polarization and one behind the EOM to filter the changed polarization out. However, there was a rest intensity of about 4 % in the guide when the light was switched off due to imperfections in the EOM and PBS. Therefore we placed behind the EOM configuration a mechnical shutter that prevented the rest light of going through the guide. Before bringing the light into the vacuum system the beam focus size had to be reduced by a telescope 50:100 mm. The beam waist in the focus was measured to be $\omega_0 \approx 150\,\mu m$. The position of the focus was aligned to be longitudinally in the middle of the guide segment. For aligning the UV beam in the transverse direction two steering mirrors were mounted on a micrometer screw tilting unit. A small fraction of light was split off by a PBS to get a quantitative measure for the position of the beam. This light was brought onto a beamsplitter and was monitored by two cameras at a different distance. The camera pictures were analyzed by a LabView program. The beam position was determined by a fit routine. Furthermore a UV photodiode was placed behind the guide to monitor the UV power behind the spectroscopy region.
The guide setup is the same as already described in section 4.1.2.

The alignment of the UV beam through the guide segment of about 20 cm length was critical. If the light was aligned sufficiently well so that first depletion signals could be seen, a special alignment procedure was done.

For that purpose a frequence scan was performed to get an overview over the line shape first at 5kV electrode voltages then at 1kV. Due to the lower electric fields and hence less broadening of the lines the zero-field-frequency was easier to estimate at lower voltages. However due to less molecular flux (5kV to 1 kV corresponds to less flux by a factor of 25) longer measurement times were necessary. After that the frequency was set between the estimated zero-field frequency and the peak maximum.

By applying now two different voltages in the two segments of the guide, a better alignment

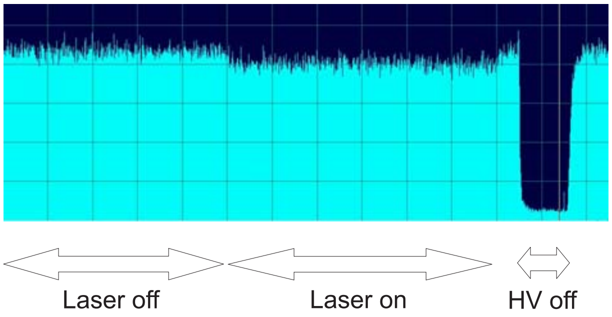

Figure 4.8: *Typical measured depletion signal. The mass spectrometer signal of ion count rate at mass of formaldehyde as function of time. The laser light is switched on during a period indicated by the middle arrow. This results in a small visible drop in the count rate. The phase with no high voltage (HV) is needed for background subtraction.*

could be achieved. In the first segment of the guide 1kV was applied. The second segment now was set to a higher voltage like 3kV or 5kV. If the filtered molecules arrive now at the second segment they see a stronger potential and are therefore radially focussed to a smaller beam. Shining in with low UV power the depletion signal was maximized by aligning the UV beam with help of the steering mirrors. The stronger molecular confinement leads to higher sensitivity in the alignment. Maximized signal corresponds then to a well aligned beam along the centre axis of the guide.

4.4.1 Measurement scheme

The measurements compared the molecular flux when no laser light was present to the flux when laser light was led through the guide. These measurements consisted of n passes (mostly n=50, 100 or 200) of a sequence with fixed laser frequency. Every sequence was 1350 ms long.

The scheme and one example of a performed sequence is depicted in Fig. 4.8. For $t = 500 - 1100$ms the laser light was switched on. A small drop in countrate is visible. From $t = 1150 - 1250$ms was the high voltage of the electrodes off. With no guiding at this time the background countrate of the mass spectrometer was measured. This is needed for backgound subtraction. With no background subtraction of the signals the depletion signal is underestimated. But due to the high countrate with 5 kV applied guide voltage this is negligible. The population measurements, however, were done at 1 kV (or even 0.5 kV) and there the effect of the background leads to a 5 % (or even 10 %) lower signal and needs to be corrected. The measurements were controlled by an AdWin system. This got its control sequence of an LabView program which provided also the graphical interface to the experimentator. The LabView program averaged also the power of the UV photodiode behind the guide in every pass. The overall averaged laser power of every measurement was needed for the power dependency measurements. The time resolved mass spectrometer signals were saved as ASCII files and were used for analyzing

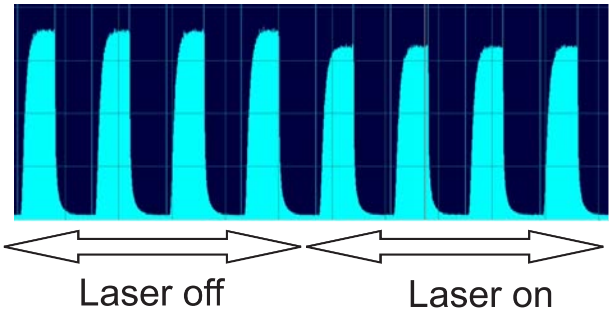

Figure 4.9: *Time-resolved mass spectrometer countrate integrated over 4000 passes. One pass takes* 1120 ms. *In the first half was the laser off, in the second half it was switched on. Eight times was HV each time for* 70 ms *switched on, visible in the guiding signals. Note the effect of the laser on the countrate.*

the measurements. The countrate with laser and without laser influence were analyzed and the loss in countrate in percent calculated. This is presented in the following chapter.

4.5 Velocity distribution measurements

Due to the possibility of individually depleting rotational states the question rose if it could be feasible to measure the velocity distribution of one state. This would be interesting, since all derived velocity distributions so far were integrated over all guided states (see Fig. 4.4). Moreover, the theoretical description with respect of longitudinal cut-off velocity (eq. 4.4) can be verified with this measurement.

The detection scheme is to measure an integrated velocity distribution with all guided states (no laser) and one when the selected state is depleted by the laser. Subtracting the latter velocity distribution from the first would result in the velocity distribution of the depleted state. Since the population of the depleted state is distributed over the range of velocities from 0 to v_{lmax} much better statistics as in the former depletion measurement is needed. The sequence for this measurement is shown in Fig. 4.9.

Chapter 5

Results and Discussion

In this chapter the results of the measurements are presented and discussed. First the lineshapes for two of the six measured lines are shown. The second section compares the measured populations to the calculated populations. Finally the velocity distribution of two states is presented in the third section.

5.1 Line shapes

The measurements started at the guided state with the highest calculated population. It is the state $|J, \tau, M\rangle = |3, 3, M\rangle$ ($M = 3, 2, 1$) whose contribution summed over M is about 14 % of the overall molecular flux at a source temperature of 150 K (see table 4.1). To get good statistics, the electrodes were set to 5 kV because the molecular flux increases quadratically with the applied voltage. Another advantage of starting at high voltage is also the expected broader line shape due to higher electric fields, which makes it easier to find first depletion signals.

In Fig. 5.1 the frequency scan of the depletion signal is shown for these measurements. The main visible peak is asymmetric and shows a maximum around 3 %. The UV power was 90 mW. The calculated zero-field frequency of the absorption spectrum fit is at $30387.9\,\mathrm{cm}^{-1}$. This is at the right rising slope of the signal, indicating that this is a transition with negative differential Stark shift. Another smaller peak with about 1 % depletion signal is visible next to the big peak. This stems probably from $|9, -3, M\rangle$ since the calculated frequency and the estimated population fits well.

It is instructive to compare directly the room-temperature spectrum, the fit of it and the measured depletion signal with each other. It is now possible to assign the two peaks in the depletion spectrum to two lines in the absorption spectrum. The third line of the absorption spectrum is neither visible in the fit nor in the depletion signal. In the latter it is hidden by the broad big peak. This becomes clear by looking at the same region with lower applied guide voltage.

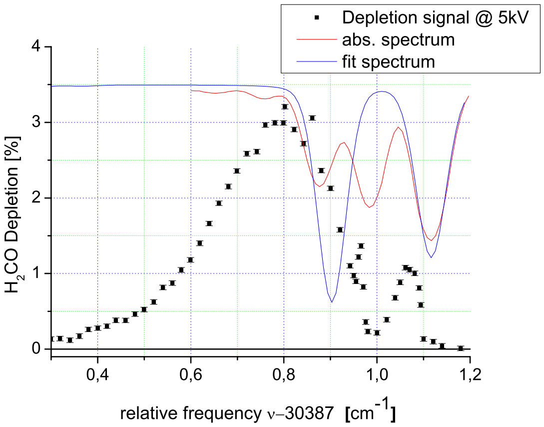

Figure 5.1: *Depletion signal in the region of the* $|3, 3, M\rangle \rightarrow |4, 2, M\rangle$ *transition. Comparison between depletion signal (black), absorption spectrum (red) and the GA fit (blue) is possible. Absorption and fit have been scaled up by a factor of 3.5 for better visibility. Relative frequency means measured frequency minus an arbitrary offset of* $30387\,\mathrm{cm}^{-1}$*. The main depletion peak is attributed to the* $|3, 3, M\rangle$ *guided state. It corresponds to the middle absorption line at* $1.0\,\mathrm{cm}^{-1}$ *of the transition* $|3, 3, M\rangle \rightarrow |4, 2, M\rangle$*. The smaller peak around 1 % agrees well with the fit line of the* $|9, -3, M\rangle \rightarrow |10, -3, M'\rangle$ *transition.*

At 2.5 kV the broadening becomes much smaller due to a lower electric field range resulting in a lower frequency Stark shift (see Fig. 5.2). Now the big peak splits up in two peak maxima. At 1 kV both peaks are separated and can be surely assigned to the two absorption lines in the room-temperature spectrum. The third peak at $\approx 1.1\,\mathrm{cm}^{-1}$ stays around 1 %. Note the increase in signal height from 5 kV to 2.5 kV and 1 kV for the two big peaks. This increase is due to the smaller electric field gradient in radial direction for lower electrode voltage. Therefore the ring width (see Fig. 4.5 a)) of adressable molecules is increased. This results in more efficient depletion of the guided state. The fact that both peaks display the same height of signal indicates that these are transitions from the same guided state (Fig. 5.2). The GA fit, however, reproduces only one transition which is between both absorption/depletion peaks and has about double intensity compared to the two absorption lines.

It is now interesting whether a fit of the line shape gives reasonable results. The measured signal at 5 kV is used for it, since the fit function developed in section 4.3.2, eq. (4.8) holds only for the nonsaturating regime. Because the interest is at the main peak, the data points which are assigned to the smaller peak are omitted. The result of the fit and the used data points are shown in Fig. 5.3. The fit agrees very well with the measured data: the shape is well reproduced. Only at the low-energy left side of the line the measured data points are slightly higher than the fit. This can be attributed to the fact that there was higher laser intensity at higher electric fields than the model assumed. This occurs if the

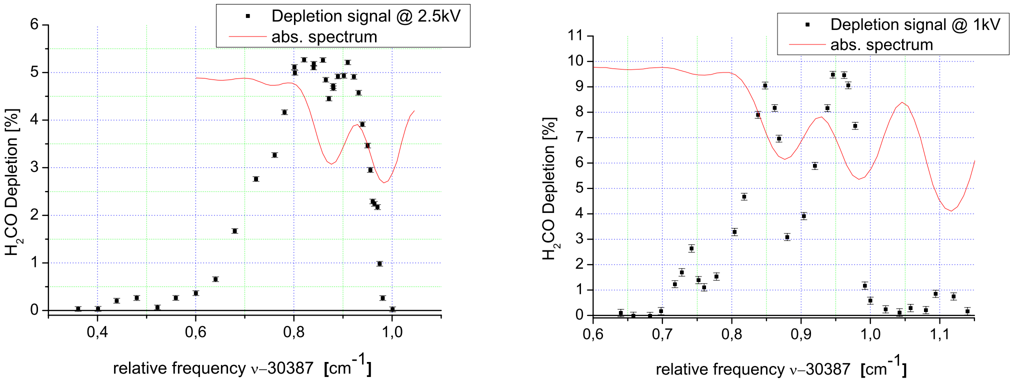

Figure 5.2: *The* $|3,3,M\rangle \rightarrow |4,2,M\rangle$ *transition for 2.5 kV and 1 kV guiding voltage (black dots). For comparison the abs. spectrum (red line) is shown (scaled for better visibility). The decreased voltage leads to less Stark-broadening of the depletion signal. The main peak splits up in two. Both peaks can be attributed to two distinct lines in the absorption spectrum.*

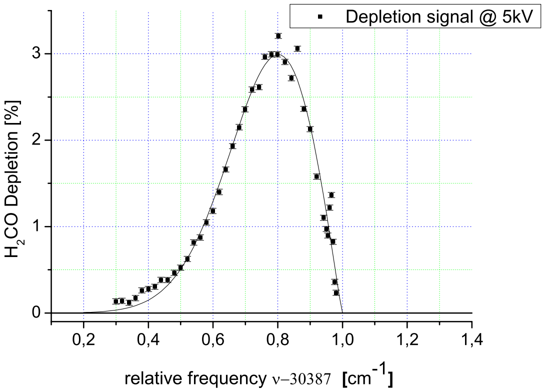

Figure 5.3: *Comparison between fit and data. The solid line is the line shape fit obtained by using the fit function derived in chapter 4 (see eq. (4.8)). The fixed parameters are:* $r_0 = 400\,\mu\mathrm{m}$ *width of molecular distribution,* $\omega_0 = 200\,\mu\mathrm{m}$ *the UV laser waist. The obtained fit parameters are: zero-field frequency* $\nu_0 = 1\,\mathrm{cm}^{-1}$*, average differential Stak shift* $\Delta W^S = -2.9\,\mathrm{cm}^{-1}/(100\mathrm{kV/cm})$ *and intensity* $\alpha = 173.9$*.*

initial state			final state	
$\lvert J,\tau,M\rangle_i$	pop$_{\mathrm{theo}}$ [%]	W^S@100kV/cm [cm^{-1}]	$\lvert J,\tau,M\rangle_f$	W^S@100kV/cm [cm^{-1}]
$\lvert 3,3,3\rangle$	8.5	2.86	$\lvert 4,3,4\rangle$	-2.1
$\lvert 3,3,2\rangle$	3.5	1.82	$\lvert 4,3,3\rangle$	-1.6
$\lvert 3,3,1\rangle$	0.7	0.81	$\lvert 4,3,2\rangle$	-1.1
			$\lvert 4,3,1\rangle$	-0.6
			$\lvert 4,3,0\rangle$	0
$\lvert 1,1,1\rangle$	4	1.28	$\lvert 2,1,2\rangle$	-1.8
			$\lvert 2,1,1\rangle$	-1.0
			$\lvert 2,1,0\rangle$	-0.2

Table 5.1: *Stark shifts of initial and final states of the transition* $\lvert 3,3,M\rangle \rightarrow \lvert 4,2,M'\rangle$ *and* $\lvert 1,1,1\rangle \rightarrow \lvert 2,1,M'\rangle$. *The transition rule* $\Delta M = 0, \pm 1$ *results in a range of possible differential Stark shifts of* $\Delta W^S = W^S_{final} - W^S_{initial} = -4.96 \cdots - 0.81\,\mathrm{cm}^{-1}$ @100 kV/cm *for* $\lvert 3,3,M\rangle$ *and* $\Delta W^S = -1.43 \cdots - 3.1\,\mathrm{cm}^{-1}$ @100 kV/cm *for* $\lvert 1,1,1\rangle$

laser is not perfectly symmetrically aligned to the guide axis. In particular the laser is also illuminating a part of the second bent segment, where it is obvious that it cannot follow the central guide axis. This leads to a higher signal for higher Stark shifted molecules. Two out of the three fit parameters can also be easily compared to expectations. The zero-field frequency $\nu_0 = 1\,\mathrm{cm}^{-1}$ deviates from the calculated $\nu_0^{fit} = 0.91\,\mathrm{cm}^{-1}$ slightly. However, the direct comparison of the room-temperature spectrum with the depletion spectrum shows excellent agreement since the middle absorption line has its peak at $0.98\,\mathrm{cm}^{-1}$.

The second parameter, which can be compared to expectations is the differential Stark shift ΔW^S. It lies in the range that is derived by the calculated differential Stark shifts of all possible involved transitions ($\Delta M = 0, \pm 1$) (see Tbl. 5.1). The third parameter α is an amplitude factor that quantifies how strong the transition is. It depends on the quality of overlap with the molecules, the strength of transition and the population.

The second studied state that is shown here is the $\lvert 1,1,1\rangle$ with a calculated population of about 4 %. It is the guided state with the lowest rotational energy. The used transition is $\lvert 1,1,1\rangle \rightarrow \lvert 2,1,M'\rangle$ ($M' = 0,1,2$). The line shape with 5 kV guide voltage applied and a fit is shown in Fig. 5.4. The shape is similar but not as broad as in the $\lvert 3,3,M\rangle$ state (Fig. 5.1). This is due to its smaller differential Stark shift. The zero-field frequency obtained from the fit is $\nu_0 = 0.41\,\mathrm{cm}^{-1}$, which agrees well with the calculated $\nu_0^{fit} = 0.39\,\mathrm{cm}^{-1}$. The differential Stark shift fit value is $\Delta W^S = -1.9\,\mathrm{cm}^{-1}/(100\,\mathrm{kV/cm})$ which lies in the range of the three possible transitions $\Delta W^S = -1.43 \cdots - 3.1\,\mathrm{cm}^{-1}/(100\,\mathrm{kV/cm})$ (see table 5.1). The line also splits up in two, as can be seen at the picture with 1kV voltage applied (see Fig. 5.5). Again the peak maxima are about the same height for both peaks. The line position in the measured room-temperature spectrum is between the two peak maxima.

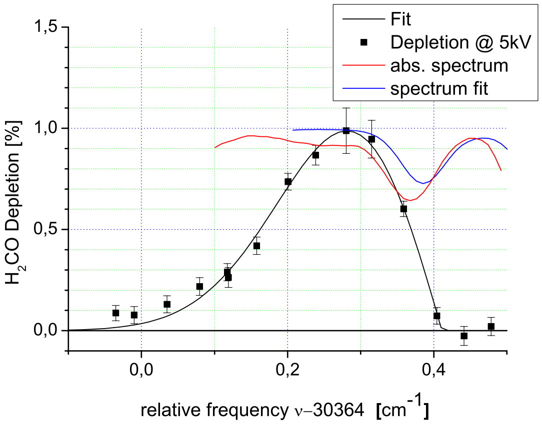

Figure 5.4: *Transition $|1,1,1\rangle \rightarrow |2,1,M'\rangle$ at 5 kV. The width is smaller due to smaller differential Stark shift compared to $|3,3,M\rangle \rightarrow |4,2,M'\rangle$ transition. The transition can be found in the absorption spectrm (red) and in the fitted spectrum (blue).*

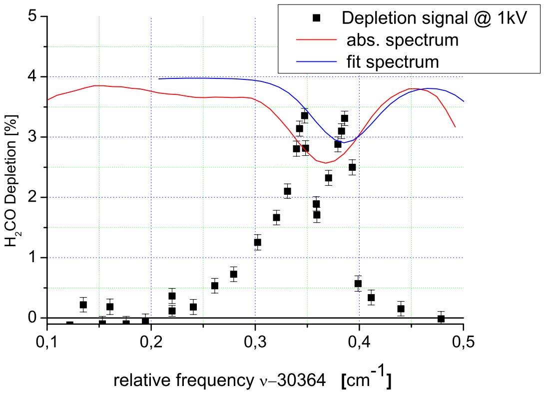

Figure 5.5: *Transition $|1,1,1\rangle \rightarrow |2,1,M'\rangle$ at 1 kV. The depletion signal splits in two lines. Contrary to the other observed linesplitting, this one cannot be found in the absorption spectrum (red line).*

5.1.1 Line splittings

The observed line splittings at states $|1,1,1\rangle$ and $|3,3,M\rangle$ for low guide voltages are somewhat surprising. At the other studied transitions a splitting did not show up. A first guess for the reason of this splitting was the fact that the M degeneracy is lifted at electric fields in the guide. But the fact that in the $|3,3,M\rangle \rightarrow |4,2,M'\rangle$ transition both peaks were clearly visible also in the room-temperature spectrum excludes this possibility, since no electric fields were present in the absorption spectroscopy. With varied guiding

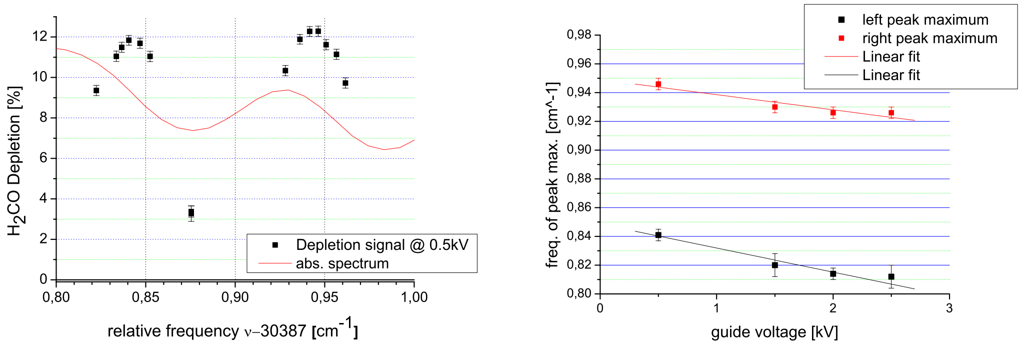

Figure 5.6: *left: $|3,3,M\rangle \rightarrow |4,2,M'\rangle$ transition region at 0.5 kV. Note the increase in peak height compared to 1 kV. right: varying the guide voltage results in shift of both peak maxima in the same manner. This indicates that both transitions have the same differential Stark shift.*

voltage the position of the peak maxima was measured to see if both peaks exhibit equal differential Stark shift. This measurement showed parallel frequency shift of the peaks meaning that they have equal differential Stark shift. This led to a extrapolated zero-field frequency splitting of $0.1\,\mathrm{cm}^{-1}$ at the $|3,3,M\rangle \rightarrow |4,2,M'\rangle$ transition (see Fig. 5.6) and $0.04\,\mathrm{cm}^{-1}$ at the $|1,1,1\rangle \rightarrow |2,1,M'\rangle$ transition. The splitting of the $|3,3,M\rangle \rightarrow |4,2,M'\rangle$ peak becomes most prominent at low guide voltage as 1 kV or even 0.5 kV (Fig. 5.6). Comparing this to the room-temperature spectrum shows that both peaks are clearly visible as distinct absorption lines. The fitted spectrum showed only one line at that position. This indicates that we have here a line splitting coming from a interaction term that is not included in the model the fit is based on. In the $|1,1,1\rangle$ state the splitting is smaller by a factor two. Furthermore, it is not visible in the room-temperature spectrum. The double peaks show in both cases the same depletion height at 1 kV. The guided initial state should therefore be the same. The vibrational modes ν_4 and ν_6 have similar energies. This leads to Coriolis coupling that could explain the observed line splitting [37].

5.2 Populations

The determination of the population was done for six rotational states. This section presents the results. The thermal reservoir was cooled to 150 K and 200 K. At 300 K two guided states were measured. For all states the measurements were done in the following way: to adress as many molecules in the state as possible, the guide voltage was reduced to 1 kV or for some measurements even to 0.5 kV. This leads to a smaller frequency shift of the molecular transitions. First the frequency of the peak maximum was determined by scanning over the line. The UV laser frequency was then fixed at peak maximum. At peak maximum the QMS loss signal was measured as a function of UV power. The resulted data was then fitted by the function (4.12) derived in section 4.3.3.

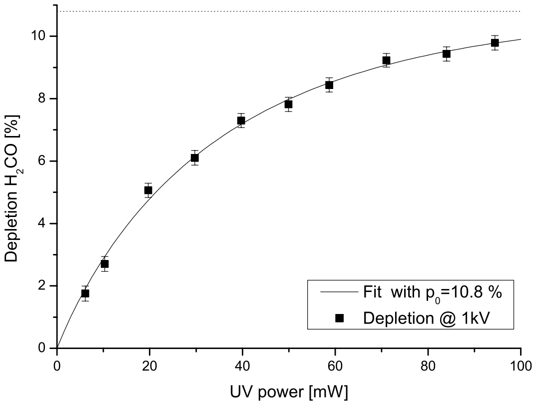

Figure 5.7: *Typical power dependency measurement. The fit (solid line) agrees well with the experimental data. The fit population parameter p_0 is here 10.8 % (dashed line) for the $|3,3,M\rangle$ state.*

$\|J,\tau,M\rangle$	$\mathrm{pop_{theo}}$ [%]	$\mathrm{pop_{exp}}$ [%]	$\Delta\mathrm{pop_{exp}}$	$\mathrm{pop_{exp}/pop_{theo}}$
$\|3,3,M\rangle$	13.8	10.8	0.5	0.78
$\|4,2,M\rangle$	9.8	8.2	0.4	0.84
$\|5,1,M\rangle$	7.1	6.0	0.4	0.85
$\|5,5,M\rangle$	5.6	4.7	0.4	0.84
$\|1,1,1\rangle$	5	3.5	0.2	0.70
$\|2,2,M\rangle$	4.5	3.5	0.3	0.77

Table 5.2: *Comparison of experimental and theoretically calculated population at 150 K source temperature. The electric field used for the calculation is $E_{max} = 20\,\mathrm{kV/cm}$ corresponding to the applied guide voltage of 1 kV. All states besides $|1,1,1\rangle$ have more than one guided M state, which sum up to the indicated population.*

The measured data of the power dependencies and the fit results for the various states are shown in the Appendix (A). One example shown for the states $|3,3,M\rangle$ with $M = 0,1,2,3$ at Fig. 5.7. The fit describes the data well. There are two resulting fit parameters (see eq. 4.12 and 4.10). One is similar to the one used in the line shape fit α. It is a measure for the efficiency of depleting this state. The second one is the actual population of this state p_0. This level is reached by the fit function in the limit of infinite laser power.

As a summary of the results of all the fits, table 5.2 shows the experimentally determined populations and the theoretical predictions at 150 K source temperature. The experimentally determined populations were all systematically smaller than calculated by 25 %. But by normalizing the measured population with respect to the highest contributing state $|3,3,M\rangle$ we have a good agreement to the relative calculated populations (see Fig. 5.8b)). The lack of 25 % could have two reasons: either not all molecules of the states could be

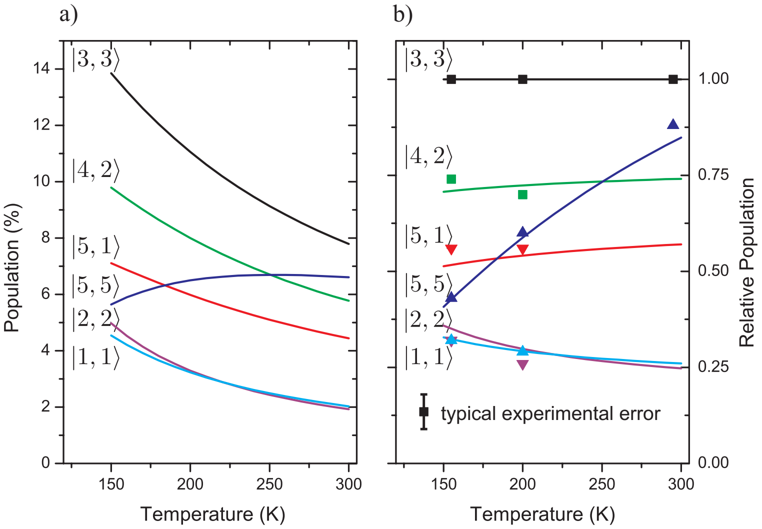

Figure 5.8: *State distribution depending on the thermal source temperature. a) Calculated distribution b) Experimental populations normalized to the* $|3, 3, M\rangle$ *state compared to the calculated populations (solid lines). Note the increase of population for the* $|5, 5, M\rangle$ *state.*

dissociated by the laser light or the molecules distribution is truly lower for the measured states than calculated. This can happen if the internal degrees of freedom are not cooled down efficiently by the thermalization body. As a result more rotational states would contribute to the flux.

With rising temperature all examined states, besides one, have a lower calculated guide population. But the behaviour of the state $|5, 5, M\rangle$ is anomalous to the other ones. Its high rotational energy of $241\,\text{cm}^{-1} \cong 330\,\text{K}$ leads to a higher thermal occupation at room-temperature compared to 150 K (see Fig. 5.8a)). Assuming that the molecules are not cooled down internally efficiently would result at 150 K in a higher population of the $|5, 5, M\rangle$ compared to the other states. This is not the case, as can be seen in Fig. 5.8b). To be sure that also for higher temperatures we measured correct relative populations we measured at 200 K source temperature and for the $|3, 3, M\rangle$ and the anomalous $|5, 5, M\rangle$ state also at room-temperature. The result of this is shown in Figure 5.8. No significant difference of theory to experimental determined populations can be seen. Furthermore the lack of 25 % persisted even at room-temperature. But at 300 K we can be sure that the molecules are thermalized also internally sufficiently long to 300 K.

Lowering the voltage from 5 kV to 1 kV increased the depletion efficiency enormously, due to lower Stark broadening. To see if the depletion is further increased, some measurements were performed at 0.5 kV. This results of course in a 75 % lower flux, so longer measurement times are needed. The result of these measurements is depicted in table 5.3. It needs to be considered that the populations are slightly different at different guide voltages. This is because the rotational states exhibit not a perfectly linear Stark shift at the trapping fields of $20 \ldots 100\,\text{kV/cm}$. The fraction $\text{pop}_{\text{exp}}/\text{pop}_{\text{theo}}$ is increased to about 85-90 %.

$\lvert J,\tau,M\rangle$	$\mathrm{pop_{theo}}$ [%]	$\mathrm{pop_{exp}}$ [%]	$\mathrm{pop_{exp}/pop_{theo}}$
$\lvert 3,3,M\rangle$	14.5	12.3	0.85
$\lvert 4,2,M\rangle$	10.2	9.5	0.94
$\lvert 5,5,M\rangle$	5.9	5.0	0.85
$\lvert 2,2,M\rangle$	4.8	4.0	0.83

Table 5.3: *Comparison of experimental and theoretically calculated population at 150 K source temperature for the depletion measurements at 0.5 kV. The electric field used for the calculation is* $E_{max} = 10\,\mathrm{kV/cm}$. *Note the slight increase in the fraction* $\mathrm{pop_{exp}/pop_{theo}}$ *compared to the 1 kV measurements at table 5.2.*

This leads to the conclusion that at 1 kV the Stark broadening still limits the depletion to about 80%.

The remaining missing 10-15 % can be attributed to two points. Firstly not all of the excited molecules do dissociate. At 330 nm at maximum a fraction of 10 % can also decay back into a electronical ground state [36]. Some of these states can still be guided and be detected by the mass spectrometer. The other possibility is given by guided molecules whose trajectories are elliptical orbits, so that they are mostly at high electric field regions and do not overlap with the laser beam. Those could become resonant if the electric field is further lowered.

5.3 Velocity distribution of rotational states

As already outlined in 4.5, velocity distributions of depleted states were measured. The first attempt used the $\lvert 3,3,M\rangle$ state with the same transition as in the earlier measurement. The dominant state is $M = 3$ with $8\,\%$ population and with a expected theoretical cut-off velocity of $v_{lmax} = 93\,\mathrm{m/s}$. The state $\lvert 3,3,2\rangle$ has $3\,\%$ population and $v_{lmax} = 76\,\mathrm{m/s}$. The third state with $M = 1$ has a negligible population. The theoretical expectation of the longitudinal velocity distribution is the sum of both distributions (compare to Fig. 4.4). The derived velocity distributions are shown in Fig. 5.9. The countrate difference of both distributions is shown on the right side and has a maximum at $v = 40\,\mathrm{m/s}$. This difference is the distribution of the depleted molecules. A large fraction of molecules with higher velocities up to $v_{lmax} = 93\,\mathrm{m/s}$ is missing compared to the expectated distribution. This can be explained by the fact that the UV laser power for this measurement with about $70\,\mathrm{mW}$ was quite low. The depletion efficiency was affected by this especially for the faster molecules due to shorter interaction time.

The second chosen state was the $\lvert 1,1,1\rangle$ state. Here only $M = 1$ is guided compared to all the other studied transitions. Therefore we deplete only one state. In this case it is expected as a result to see a pronounced cut-off velocity. The two obtained velocity distributions are shown at the left of Fig. 5.10 (red/blue: laser off/on). Here the average laser power was about $85\,\mathrm{mW}$. The measurement also had much better statistics.

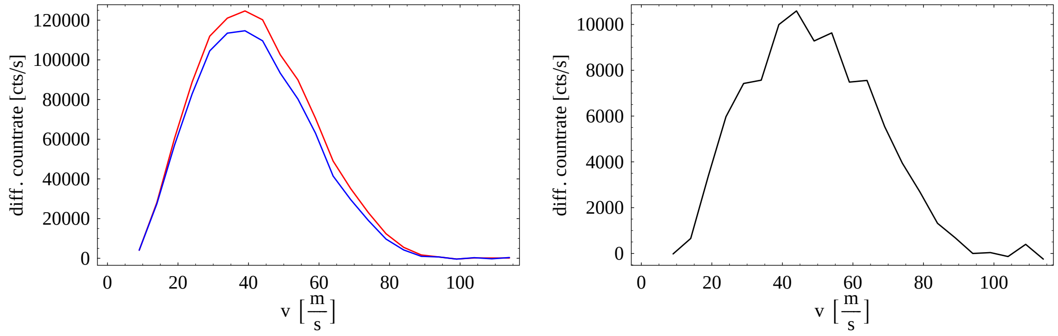

Figure 5.9: *Left: two velocity distributions are shown. The red line corresponds to no depletion, the blue is obtained by depleting the* $|3,3,M\rangle$ *states (M=1, 2, 3). Right: difference of both velocity distributions; it should correspond to the velocity distribution of the depleted states. It shows a similar shape as the total velocity distribution. The expected cut-off is at* $v_{lmax} = 93\,\mathrm{m/s}$. *The depletion effiency was probably too low since the laser power was not sufficiently high. The velocity binning is* $5\,\mathrm{m/s}$. *Statistical fluctuations are bigger for smaller binning.*

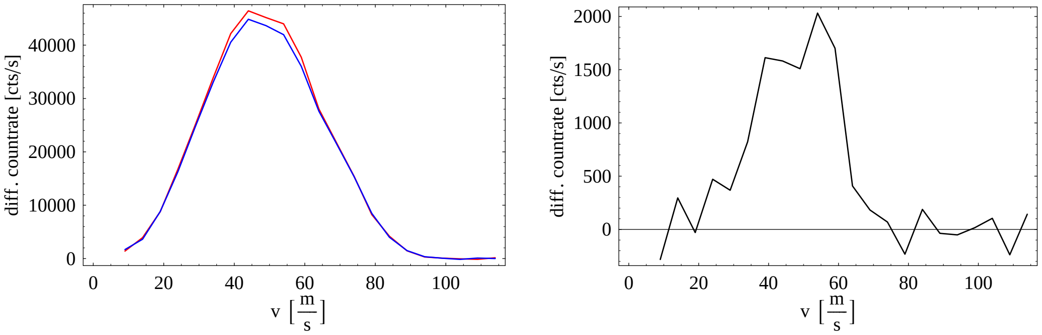

Figure 5.10: *The same as in 5.9 but here for the* $|1,1,1\rangle$ *state with a lower Stark shift. The velocity distribution of the depleted molecules shows a sharp edge between* $60-70\,\mathrm{m/s}$. *The theoretical limit is* $v_{lmax} = 67\,\mathrm{m/s}$. *The velocity binning is* $4\,\mathrm{m/s}$. *Statistical fluctuations are bigger for smaller binning.*

At the peak maximum a smaller value is visible for the blue line. The integrated count rate difference between the red and the blue curve is about 2.8%. The difference of both velocity distributions shows an edge between $60-70\,\mathrm{m/s}$. The calculated position should be at $v_{lmax} = 67\,\mathrm{m/s}$, assuming a Stark shift of $0.3\,\mathrm{cm}^{-1}$ at $E_{max} = 17\,\mathrm{kV}$ maximum electric field. This is in excellent agreement with the measurement.

Chapter 6

Conclusion and Outlook

In this thesis a new technique is developed and applied to measure the rotational state distribution of a velocity-filtered beam of formaldehyde. This method induces electronic transitions in a guided molecular beam in a rotationally-resolved way. The excited molecules are lost and the rotational state is hence depleted.

To address the guided states individually, precise knowledge of the transition frequencies is needed. For this purpose room-temperature spectroscopy has been performed. Two vibrational bands have been measured rotationally-resolved with a resolution much higher than in previously published measurements. The spectrum has been fitted resulting in improved molecular constants of formaldehyde, making it possible to address the guided states. The depletion measurements have been understood qualitatively and quantitatively by deriving a theoretical model of the observed lineshape and power dependency of the signal, which describes the measured data well. It is shown that states could be depleted almost completely according to the calculated contribution. The measured populations of the states agree well with the calculated populations. It is shown that the six studied states make up about 30 % of the total molecular flux of the guide. This demonstrates that the guide is a powerful tool to supply a high fraction of molecules in a handful of rotational states that can be used for future studies.

It is planned to apply the technique to a quadrupole guide with a cryogenically cooled thermal source. This experiment is set up at the Rempe group and provides a beam of guided molecules with an expected high purity due to the low thermal source temperature of about 5 K. This can now be confirmed experimentally using the new technique.

Furthermore, the line assignment in absorption spectra can be cross-checked using the guide population as another parameter. Another application are measurements of weak transitions, since the interaction time with the laser is much increased compared to convential molecular beam spectroscopy. However, the electric field in the quadrupole guide shifts the resonance frequency via the Stark effect, which decreases the frequency resolution and depletion efficiency of the measurements. Using for example a hexapole instead of the quadrupole guide, decreases the electric field effect, since the electric field strength rises radially quadratically instead of linear. Another advantage compared to supersonic molecular beam spectroscopy is the fact that also higher J states are occupied in the guide. These high-J states are not present at supersonic molecular beams, since also internal degrees of freedom are cooled in the adiabatic beam expansion.

Appendix A

Absorption spectra

The spectroscopy measurements (black) of the two vibrational bands $2^1_0 4^3_0$ and $2^2_0 4^1_0$ are shown together with the simulated spectrum (blue).

A.1 Absorption spectrum of the $2^1_0 4^3_0$ vibration band

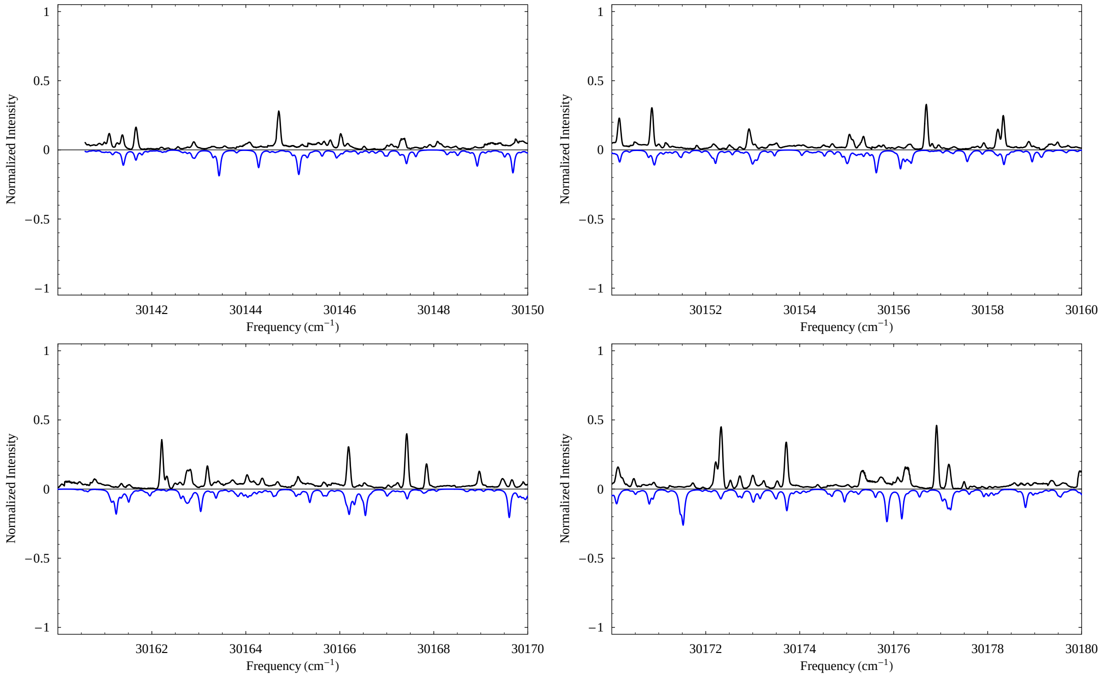

Figure A.1: *Measured (black) and simulated spectrum (blue). Arranged up and down, respectively, for better visibility.*

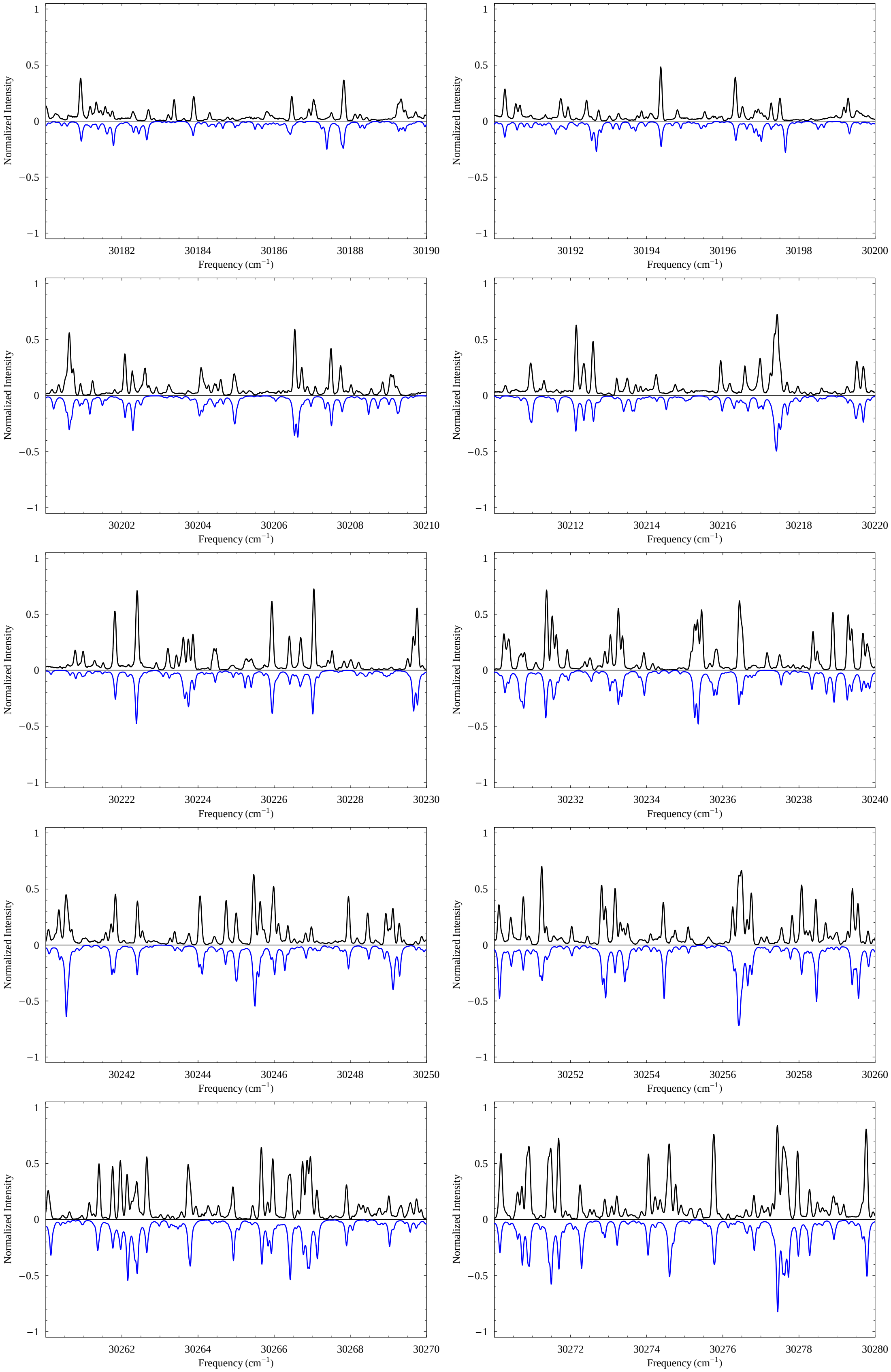

Figure A.2: *Absorption spectrum*

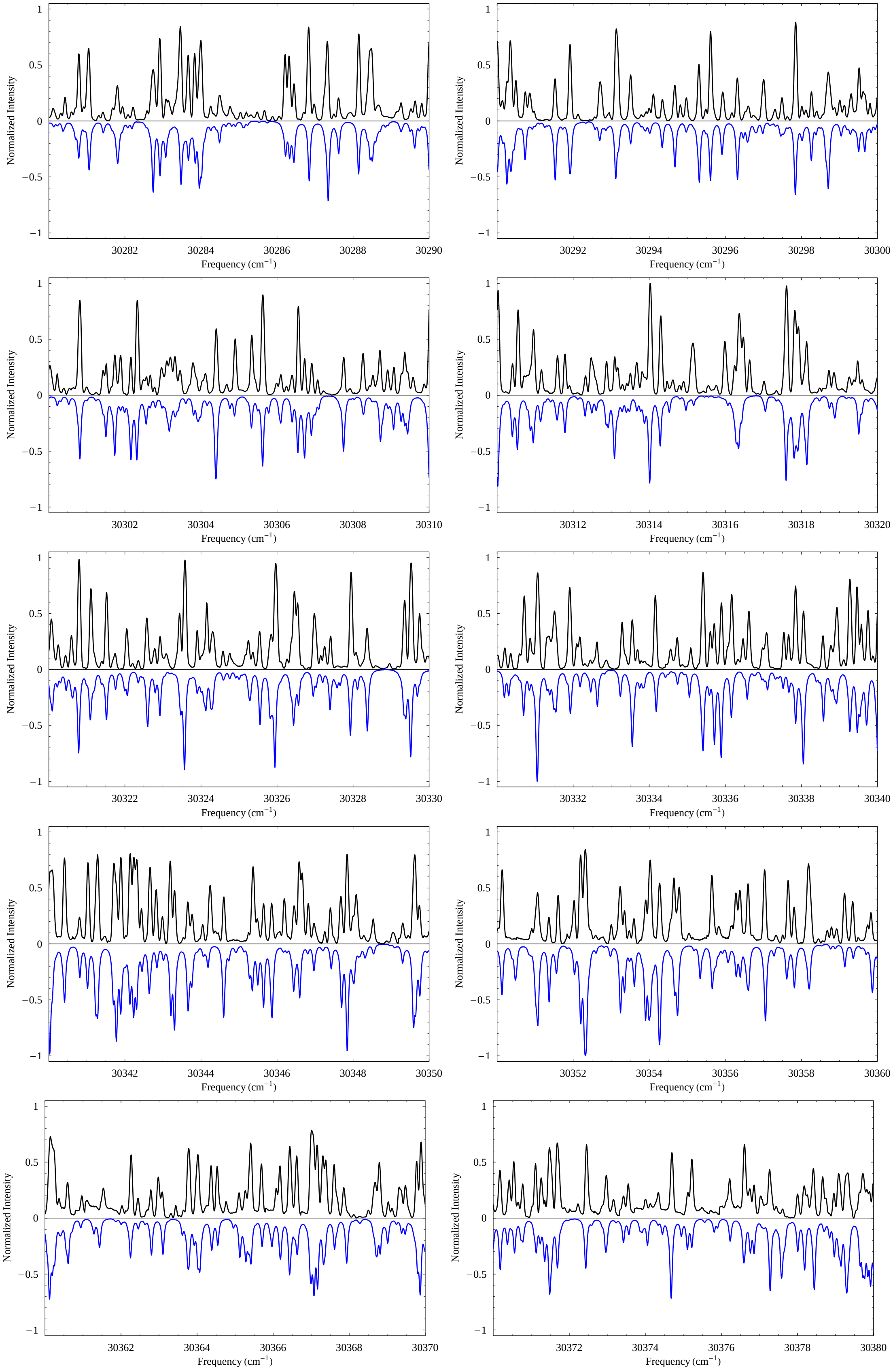

Figure A.3: *Absorption spectrum*

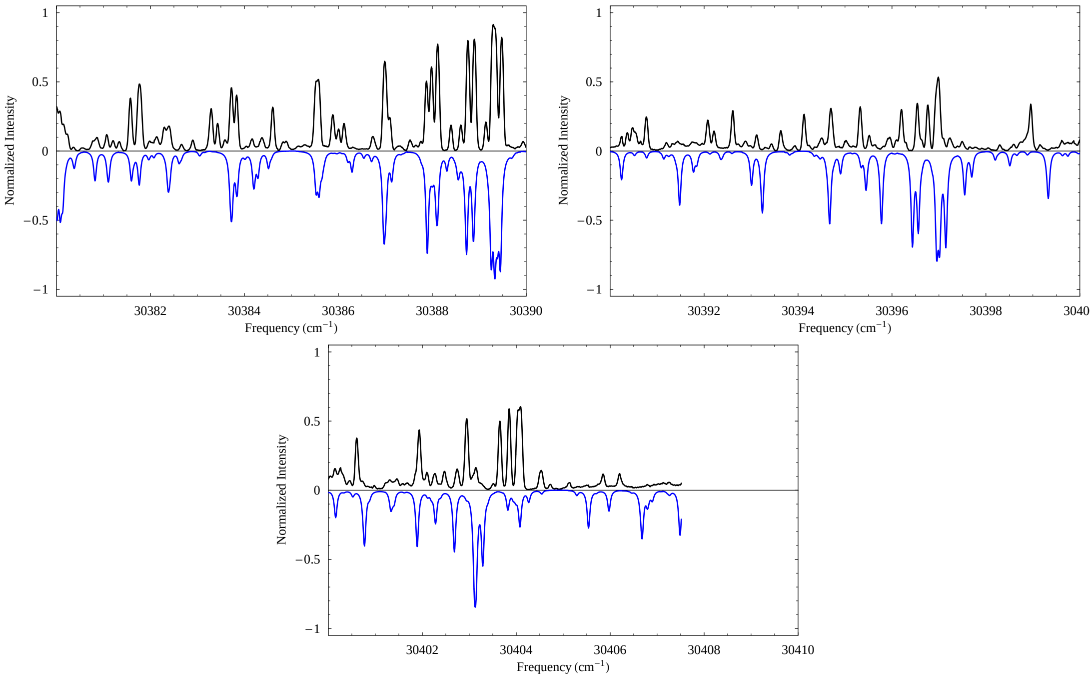

Figure A.4: *Absorption spectrum*

A.2 Absorption spectrum of the $2_0^2 4_0^1$ vibration band

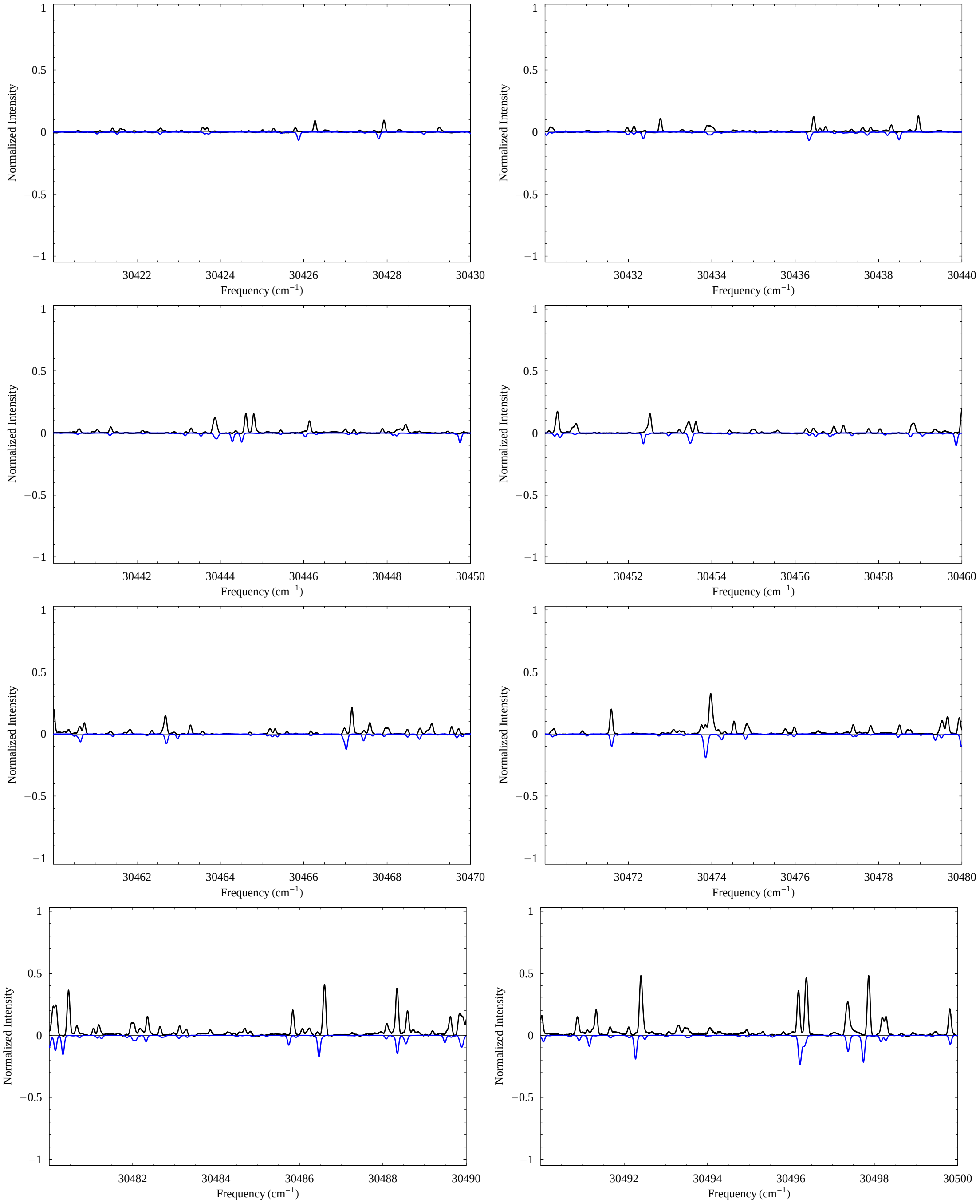

Figure A.5: *Measured (black) and simulated spectrum (blue). Arranged up and down, respectively, for better visibility.*

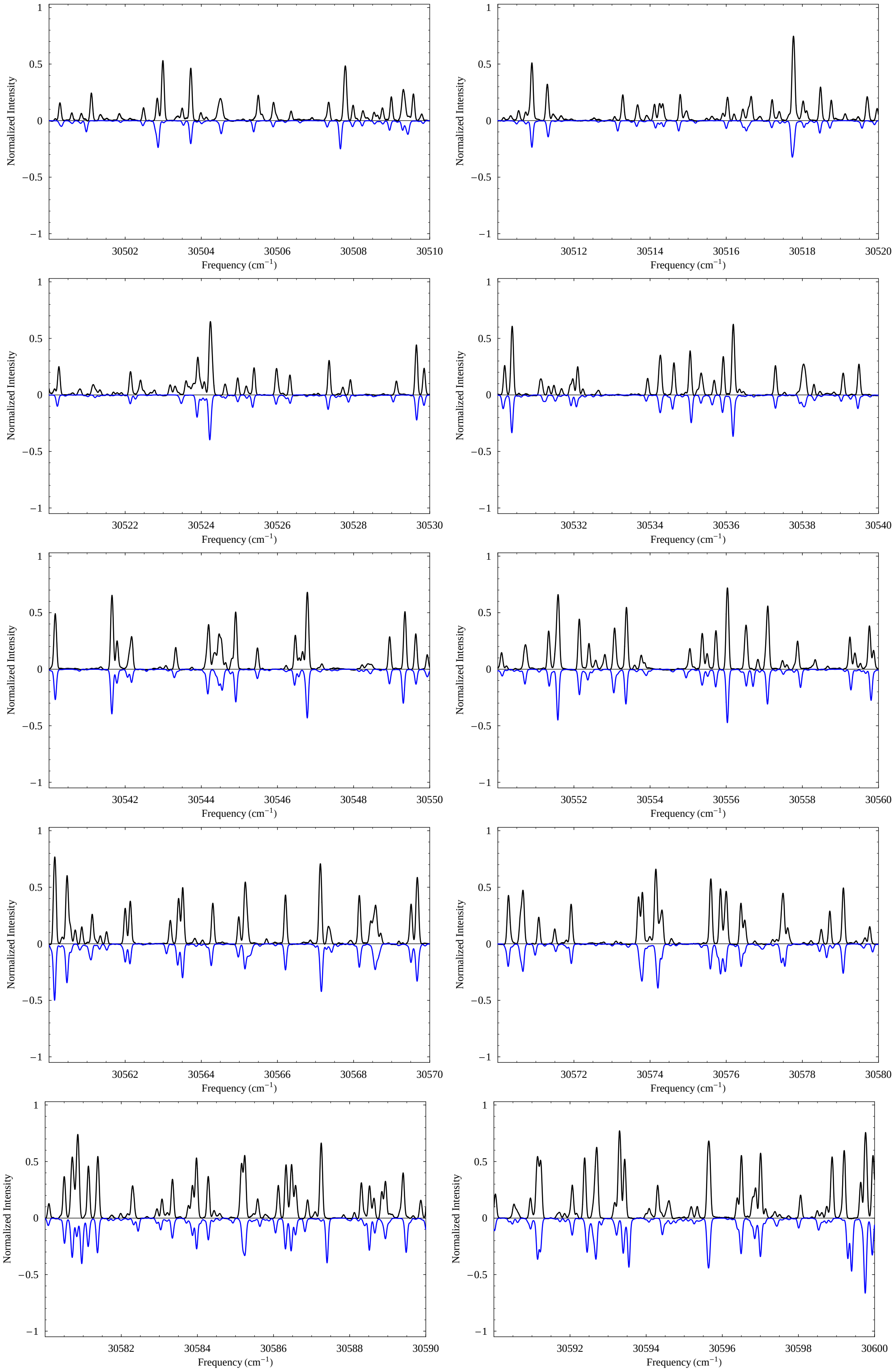

Figure A.6: *Absorption spectrum*

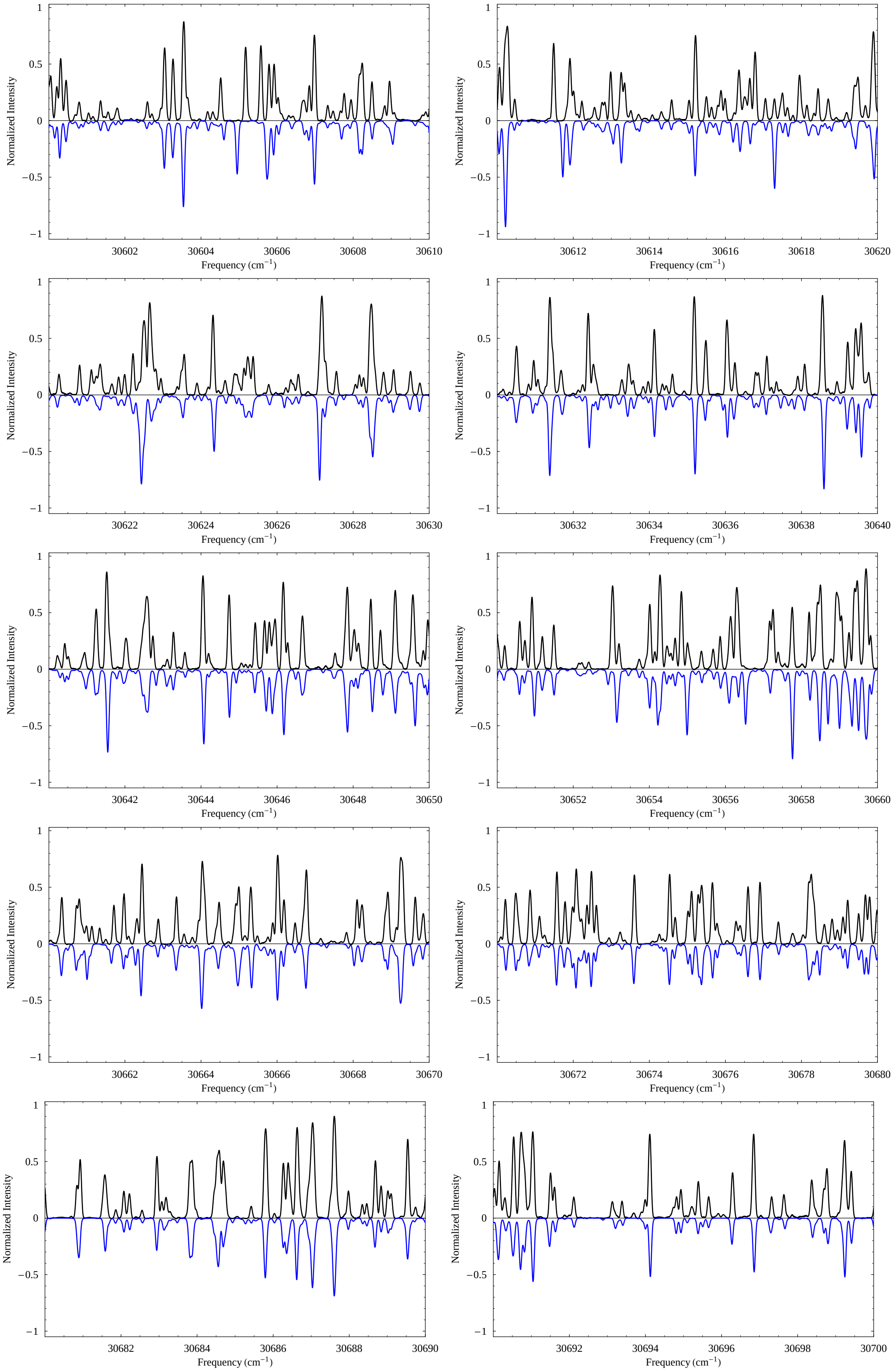

Figure A.7: *Absorption spectrum*

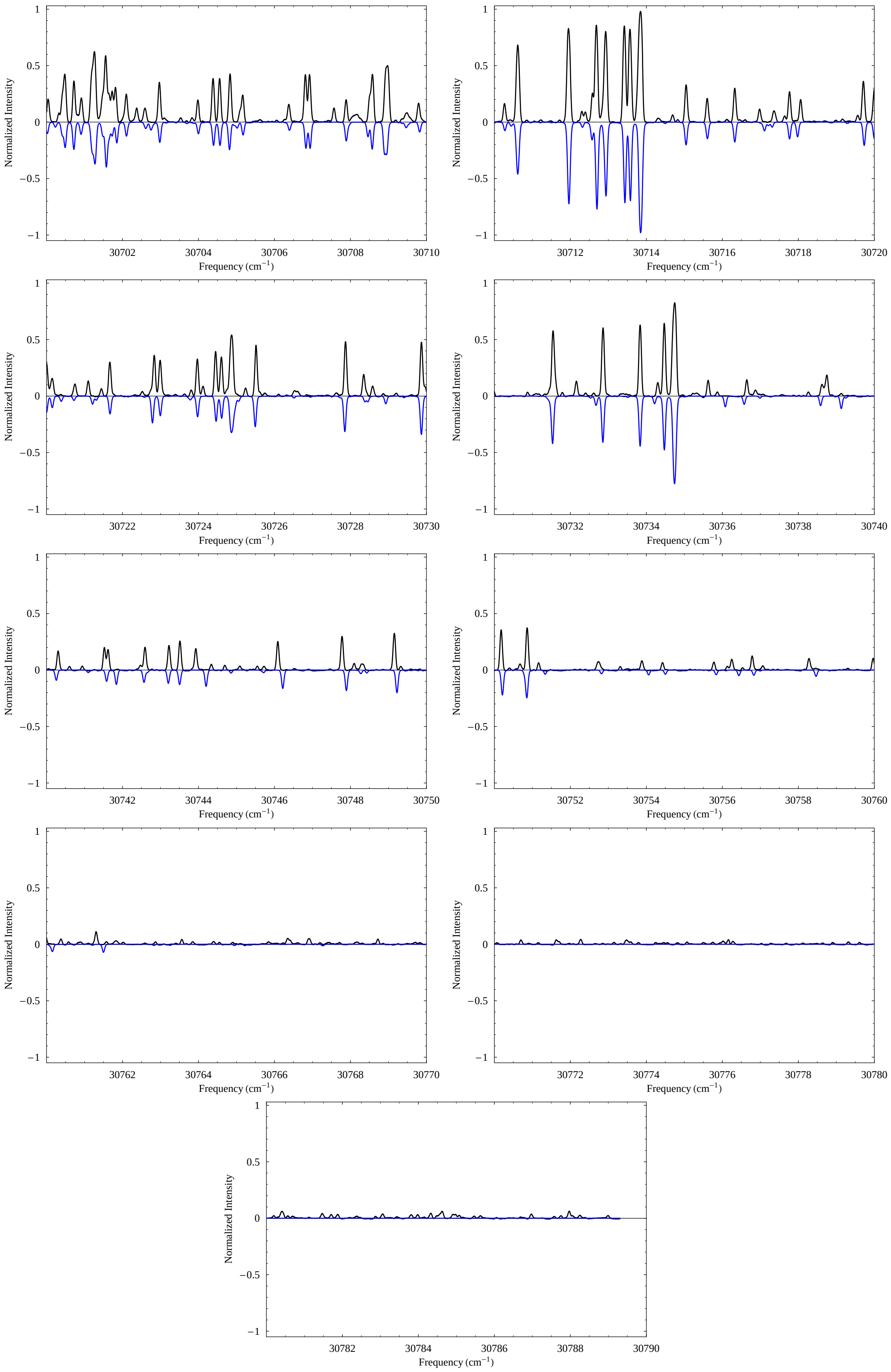

Figure A.8: *Absorption spectrum*

Appendix B

Power dependencies

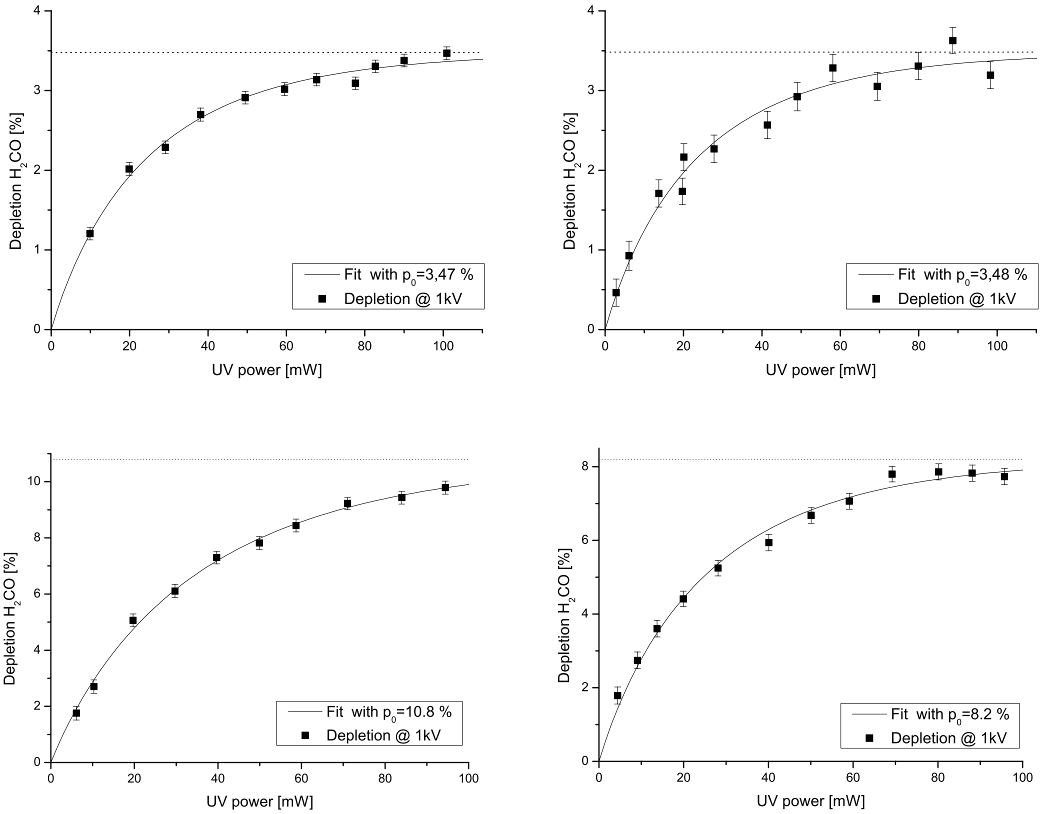

Figure B.1: *Power dependency measurements of the states. From top left to bottom right they are:* $|1,1,1\rangle$, $|2,2,M\rangle$, $|3,3,M\rangle$, $|4,2,M\rangle$. *Measured at 1 kV guide voltage and 150 K source temperature. The transitions are listed in Tbl. 3.1.*

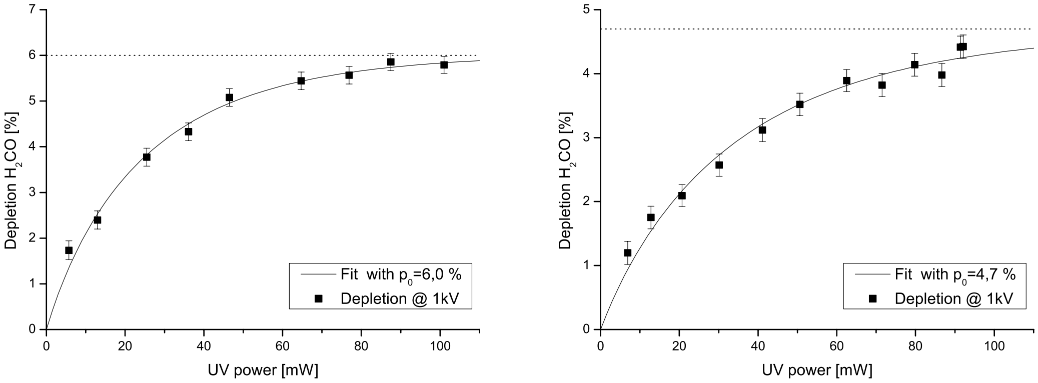

Figure B.2: *Power dependency measurements of the states. From left to right they are:* $|5,1,M\rangle$, $|5,5,M\rangle$. *The data is measured at 1 kV guide voltage and 150 K source temperature. The transitions are listed in Tbl. 3.1.*

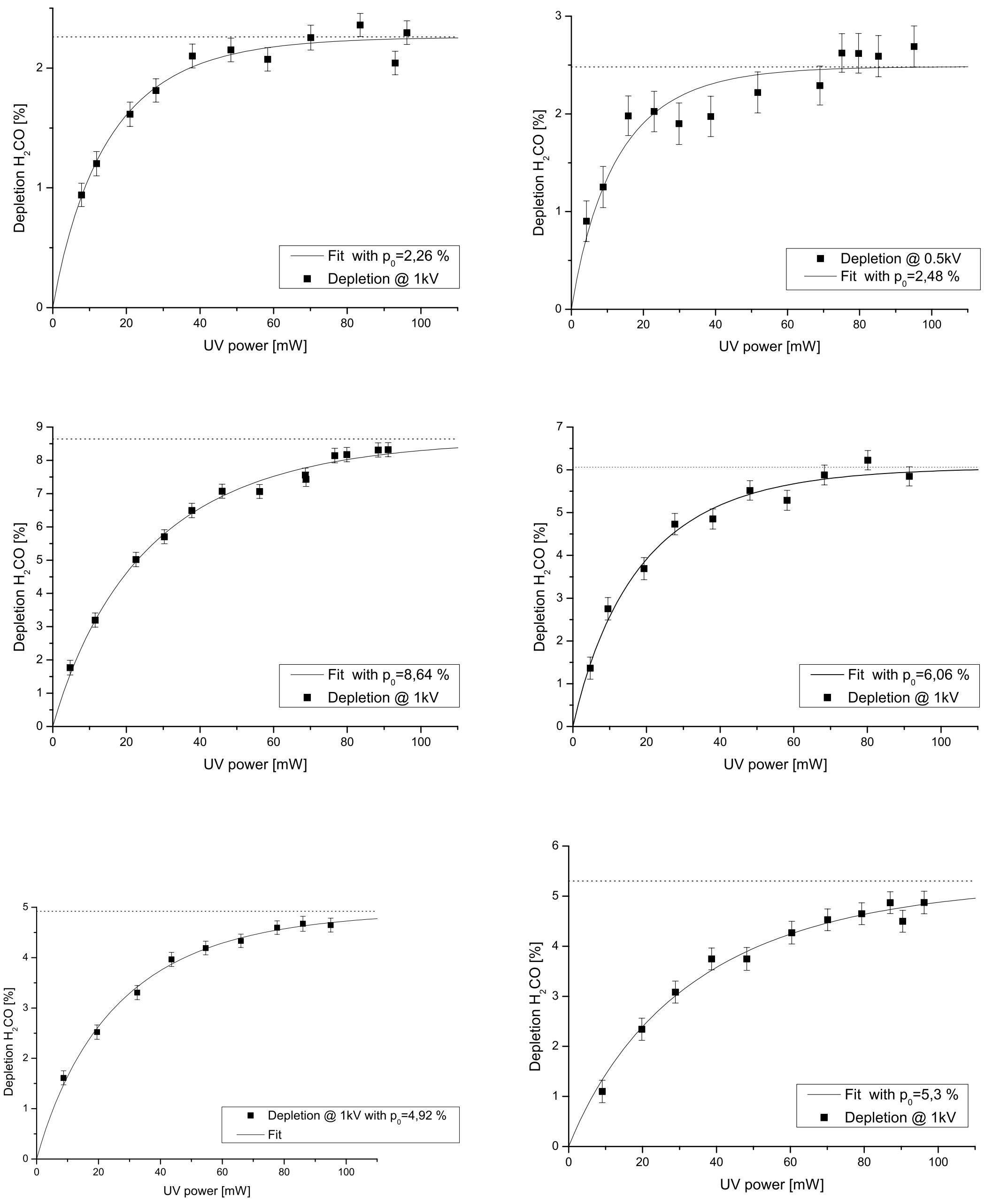

Figure B.3: *Power dependency measurements of the states. From top left to bottom right they are:* $|1,1,1\rangle$, $|2,2,M\rangle$, $|3,3,M\rangle$, $|4,2,M\rangle$, $|5,1,M\rangle$, $|5,5,M\rangle$. *The data is measured at 1 kV guide voltage and 200 K source temperature. State* $|2,2,2\rangle$ *has been measured at 0.5 kV. The transitions are listed in Tbl. 3.1.*

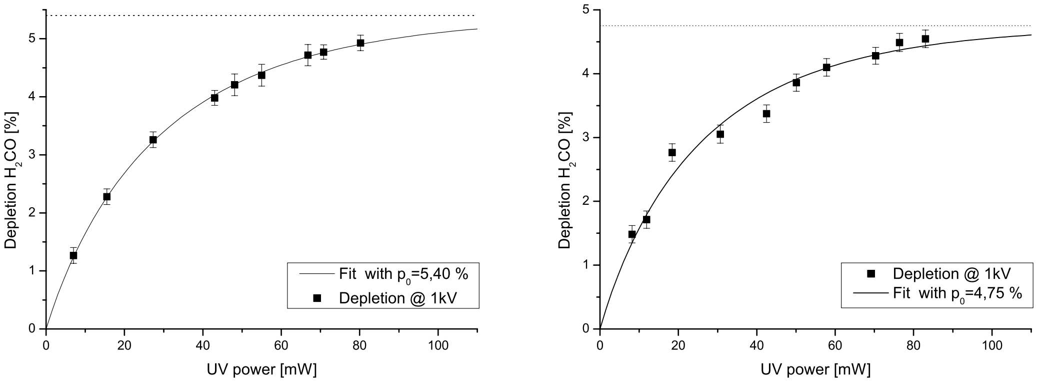

Figure B.4: *Power dependency measurements of the states. Left is* $|3,3,M\rangle$*, right is* $|5,5,M\rangle$*. The data is measured at 1 kV guide voltage and 300 K source temperature. The transitions are listed in Tbl. 3.1.*

Bibliography

[1] M. H. Anderson, J. R. Ensher, M. R. Matthews, C. E. Wiemann, and E. A. Cornell. Observation of Bose-Einstein condensation in a dilute atomic vapor. *Science*, 269:198, 1995.

[2] B. C. Regan, E. D. Commins, C. J. Schmidt, and D. DeMille. New Limit on the Electron Electric Dipole Moment. *Phys. Rev. Lett.*, 88:071805, 2002.

[3] J.J. Hudson, B.E. Sauer, M.R. Tarbutt, and E.A. Hinds. Measurement of the electron electric dipole moment using Ybf molecules. *Phys. Rev. Lett.*, 89:89(2):3003, 2002.

[4] D. DeMille, F. Bay, S. Bickman, D. Kawall, Jr. D. Krause, S. E. Maxwell, and L. R. Hunter. Investigation of PbO as a system for measuring the electric dipole moment of the electron. *Phys. Rev. A*, 61(05):2507, 2000.

[5] N. Syassen, D.M. Bauer, M. Lettner, D. Dietze, T. Volz, S. Dürr, and G. Rempe. Atom-molecule Rabi oscillations in a Mott insulator. *Phys. Rev. Lett.*, 99:033201, 2007.

[6] D. DeMille. Quantum computation with trapped polar molecules. *Phys. Rev. Lett.*, 88(06):7901, 2002.

[7] H. P. Buchler, A. Micheli, and P. Zoller. Three-body interactions with cold polar molecules. *Nature Physics*, 3:726–731, 2007.

[8] J. T. Bahns, W. C. Stwalley, and P. L. Gould. Laser cooling of molecules: A sequential scheme for rotation, translation, and vibration. *The Journal of Chemical Physics*, 104(24):9689–9697, 1996.

[9] G. Morigi, P.W.H. Pinkse, M. Kowalewski, and Regina de Vivie-Riedle. Cavity cooling of internal molecular motion. *Phys. Rev. Lett.*, 99:073001, 2007.

[10] Vladan Vuletić and Steven Chu. Laser cooling of atoms, ions, or molecules by coherent scattering. *Phys. Rev. Lett.*, 84:3787 – 3790, 2000.

[11] A. Fioretti, D. Comparat, A. Crubellier, O. Dulieu, F. Masnou-Seeuws, and P. Pillet. Formation of Cold Cs_2 Molecules through Photoassociation. *Phys. Rev. Lett.*, 80:4402, 1998.

[12] E. A. Donley, N. R. Claussen, S. T. Thompson, and C. E. Wieman. Atom-molecule coherence in a Bose-Einstein condensate. *Nature*, 417:529, 2002.

[13] M. Greiner, C. A. Regal, and D. S. Jin. Emergence of a molecular Bose-Einstein condensate from a Fermi gas. *Nature*, 426:537, 2003.

[14] J.D. Weinstein, R. DeCarvalho, T. Guillet, B. Friedrich, and J.M. Doyle. Magnetic trapping of calcium monohydride molecules at millikelvin temperatures. *Nature*, 395(6698):148–50, 1998.

[15] H.L. Bethlem, F.M.H. Crompvoets, R.T. Jongma, Sebastiaan Y.T. van de Meerakker, and Gerard Meijer. Deceleration and trapping of ammonia using time-varying electric fields. *Phys. Rev. A*, 65:053416, 2002.

[16] R. Fulton, A. I. Bishop, M. N. Schneider, and P. F. Barker. Optical stark deceleration of nitric oxide and benzene molecules using optical lattices. *J. of Physics B*, 39:1097–1109, 2006.

[17] W. Demtröder. *Molekülphysik*. Oldenbourg Verlag, 2003.

[18] J.K.G. Watson. Determination of centrifugal distortion coefficients of asymmetric-top molecules. *J. Chem. Phys.*, 46(5):1935, 1967.

[19] C.A. Cantrell, J.A. Davidson, A.H. McDaniel, R.E. Shetter, and J.G. Calvert. Temperature-dependent formaldehyde cross sections in the near-ultraviolet spectral region. *J. Phys. Chem.*, 94(10):3902–3908, 1990.

[20] W. Demtröder. *Laserspectroscopy*. Springer, Heidelberg, 2003.

[21] W. Demtröder. *Experimentalphysik 3, Atome, Moleküle und Festkörper*. Springer, Berlin, 2 edition, 2000.

[22] M. Zeppenfeld, M. Motsch, P.W.H. Pinkse, and Gerhard Rempe. Doppler-free spectroscopy of weak transitions: An analytical model applied to formaldehyde. *arxiv:physics*, 0708:0784, 2007.

[23] R. Spence and W. Wild. The preparation of liquid monomeric formaldehyde. *J. Chem. Soc.*, pages 338 – 340, 1935.

[24] C.A. Smith, F.D. Pope, B. Cronin, C.B. Parkes, and A.J. Orr-Ewing. Absorption cross sections of formaldehyde at wavelengths from 300 to 340nm at 294 and 245k. *J. Phys. Chem. A*, 110:11645–11653, 2006.

[25] James K.G. Watson. Determination of centrifugal-distortion coefficients of asymmetric-top molecules. iii. sextic coefficients. *J. Chem. Phys.*, 48(10):4517, 1968.

[26] W.L. Meerts and M. Schmitt. A new automated assign and analysing method for high-resolution rotationally resolved spectra using genetic algorithms. *Phys. Scripta*, 73:C47–C52, 2006.

[27] E.C. Apel and E.K.C. Lee. Electronic spectra and single rotational level fluorescence lifetimes of jet-cooled H_2CO: The $\tilde{a}^1a_2 \leftarrow \tilde{x}^1a_1$ $2^1_0 6^1_0$, $2^1_0 4^3_0$, $2^1_0 4^1_0 6^1_0$. *J. Phys. Chem.*, 59:1391, 1985.

[28] D.J. Clouthier and D.A. Ramsay. The spectroscopy of formaldehyde and thioformaldehyde. *Ann. Rev. Phys. Chem.*, 34:31–58, 1983.

[29] S.A. Rangwala, T. Junglen, T. Rieger, P.W.H. Pinkse, and G. Rempe. Continuous source of translationally cold dipolar molecules. *Phys. Rev. A*, 67:043406, 2003.

[30] T. Junglen. Guiding and trapping of cold dipolar molecules. *Dissertation*, 2006.

[31] G.W. King, R.M. Hainer, and P.C. Cross. The asymmetric rotor, i. calculation and symmetry classification of energy levels. *J. Chem. Phys.*, 11:27, 1943.

[32] T. Junglen, T. Rieger, S.A. Rangwala, P.W.H. Pinkse, and G. Rempe. Slow ammonia molecules in an electrostatic quadrupole guide. *Eur. Phys. J. D*, 31:365–373, 2003.

[33] T. Rieger, T. Junglen, S.A. Rangwala, G. Rempe, P.W.H. Pinkse, and J. Bulthuis. Water vapour at a translational temperature of 1 K. *Phys. Rev. A*, 73:061402, 2006.

[34] T. Junglen, T. Rieger, S.A. Rangwala, P.W.H. Pinkse, and G. Rempe. Two-dimensional trapping of dipolar molecules in time-varying electric fields. *Phys. Rev. Lett.*, 92:223001, 2004.

[35] T. Rieger, T. Junglen, S.A. Rangwala, P.W.H. Pinkse, and G. Rempe. Continuous loading of an electrostatic trap for polar molecules. *Phys. Rev. Lett.*, 95:173002, 2005.

[36] C.B. Moore and J.C. Weisshaar. Formaldehyde photochemistry. *Ann. Rev. Phys. Chem.*, 34:525–555, 1983.

[37] S.K. Gray and M. J. Davis. Coriolis induced vibration and rotation mixing in formaldehyde. *J. Chem. Phys.*, 90:10, 1989.

Danksagung

An dieser Stelle möchte ich allen danken, die das Zustandekommen dieser Arbeit in vielfältigster Weise unterstützt haben.

- Zuallererst danke ich Prof. Gerhard Rempe für das Ermöglichen dieses Projektes und für die Aufnahme in diese hochmotivierte (und motivierende) Gruppe.
- Prof. Andreas Tünnermann möchte ich für die Bereitschaft als betreuender Professor von Jenaer Seite zur Verfügung zu stehen und für die unbürokratische und hilfsbereite Zusammenarbeit danken.
- Dr. Pepijn Pinkse danke ich für die Unterstützung während der Arbeit, insbesondere in der Endphase.
- Meinem betreuenden Doktoranden Michael Motsch danke ich für die bereitwilligen Erklärungen auch kompliziertester "Rotor-Fälle", für die fürsorgliche Versorgung meiner Parkplatz-Verletzung und für seine offene und ehrliche Art.
- Christian Sommer, Laurens van Buuren, Martin Zeppenfeld, Michael Motsch, Pepijn Pinkse, Sebastian Pohle und Thomas Rieger danke ich insgesamt für die nette Athmosphäre bei den "Molekülis".
- Den Technikern Josef Bayerl, Franz Denk und Helmuth Stehbeck und dem Elektroniker Tom Wiesmeier (ich werde einen Kuhdrahtzaun nur auf einem Bein anfassen ;-)) möchte ich hier auch meinen herzlichen Dank ausdrücken, sie haben auch durch ihr Know-how so einiges zum Gelingen der Arbeit beigetragen.
- Der gesamten Rempe-Gruppe danke ich für interessante Gespräche, stetige Hilfsbereitschaft, nette Kicker-Runden, Nacht-Rodeln und und und...
- Meinem Studienfreund Bastian Schröter danke ich für eine schöne Zeit.
- Den ganzen lieben Menschen aus Jena, die ich in den vier Jahren kennengelernt haben, möchte ich meinen Dank aussprechen für eine tolle, lustige und spannende Studienzeit.
- Meiner Familie die mich auf ganz unterschiedliche Weise unterstützten und motivierten danke ich hiermit, denn ohne sie wäre ich jetzt nicht hier.

All denjenigen, die hier unerwähnt bleiben, die mich aber nichtsdestotrotz unterstützten möchte ich ebenfalls mein Dankeschön ausdrücken.